LEVEL II

② ℋ

AD A057057

AD No.
DDC FILE COPY

UNDERSEA

RESEARCH

CORPORATION

7777 Leesburg Pike, Suite 306

Falls Church, Virginia 22043 • (703) 790-1970

LEVEL

AN ANALOG FFT BEAMFORMER

FOR ACOUSTIC APPLICATIONS

Final rept. 15 Feb 77-14 Apr 78,
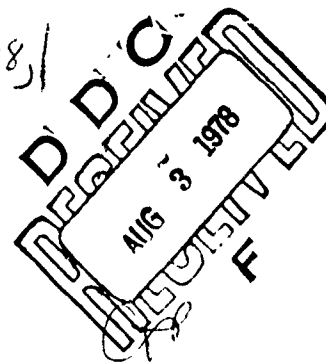
Final Report

21 March 1978

Contract Number N00014-77-C-0494

Prepared By

UNDERSEA RESEARCH CORPORATION
7777 Leesburg Pike, Suite 306
Falls Church, Virginia 22043

Prepared For

OFFICE OF NAVAL RESEARCH
Department of the Navy
800 North Quincy Street
Arlington, Virginia 22217

REPORT DOCUMENTATION PAGE		READ INSTRUCTIONS BEFORE COMPLETING FORM
1. REPORT NUMBER	2. GOVT ACCESSION NO.	3. RECIPIENT'S CATALOG NUMBER
4. TITLE (and Subtitle) An Analog FFT Beamformer for Acoustic Applications		5. TYPE OF REPORT & PERIOD COVERED FINAL 15 Feb 77 — 14 Apr 78
		6. PERFORMING ORG. REPORT NUMBER
7. AUTHOR(s)		8. CONTRACT OR GRANT NUMBER(s) N00014-77-C-0494
9. PERFORMING ORGANIZATION NAME AND ADDRESS Undersea Research Corporation 7777 Leesburg Pike, Suite 306 Falls Church, Virginia 22043	391 926	10. PROGRAM ELEMENT, PROJECT, TASK AREA & WORK UNIT NUMBERS
11. CONTROLLING OFFICE NAME AND ADDRESS Office of Naval Research Department of the Navy 800 North Quincy Street Arlington, Virginia 22217		12. REPORT DATE 21 March 1978
		13. NUMBER OF PAGES 102
14. MONITORING AGENCY NAME & ADDRESS(If different from Controlling Office) Same as #11		15. SECURITY CLASS. (of this report)
		15a. DECLASSIFICATION/DOWNGRADING SCHEDULE

16. DISTRIBUTION STATEMENT (of this Report)

Unlimited

17. DISTRIBUTION STATEMENT (of the abstract entered in Block 20, if different from Report)

Unlimited

18. SUPPLEMENTARY NOTES

19. KEY WORDS (Continue on reverse side if necessary and identify by block number)

Beamformer
Acoustic Imaging
Focusing
Fast Fourier Transform

20. ABSTRACT (Continue on reverse side if necessary and identify by block number)

An analog FFT beamformer has been designed, built and tested for one- and two-dimensional arrays. In addition, a focusing capability has been built and tested. The focusing system is used to remove the signal wavefront curvature due to close sources.

This technology is applicable to a wide variety of array configurations, providing beamformers that are inexpensive, reliable, small, low power and have high data throughput rates.

DD FORM 1473 EDITION OF 1 NOV 65 IS OBSOLETE
1 JAN 73

CONTENTS

iii

FIGURES

TABLES

1. INTRODUCTION

The purpose of this report is to document the theory of operation, operating characteristics, implementation and test of a beamforming technology developed in an Office of Naval Research program. The technology is an analog FFT beamformer implemented with operational amplifiers, resistors and capacitors that can be used to implement beamformers of $2^m 3^n 5^p$ by $2^q 3^r 5^s$ channels. These beamformers can be made inexpensive, reliable, small and low power. In addition, being analog, these beamformers have a very high data throughput rate, and have been demonstrated as acoustic imaging systems.

An analog focusing circuit has also been built and tested. The purpose of the focusing circuit is to remove the curvature from the received signal caused by a close source, prior to beamforming.

This technology development first began in 1973 at The Catholic University of America in Washington, D.C., where a 16x16 channel two-dimensional analog FFT beamformer was designed and built. Bendix Corporation's Electrodynamics Division built a square 16x16 hydrophone array, and the two equipments were interfaced and tested in the water by the Applied Research Laboratories of the University of Texas during 1974, 1975 and 1976. The results of these tests were documented as motion pictures of passive moving targets. During 1976 Catholic University also built printed circuit cards for a 1x64 beamformer with focusing.

In 1977 and early 1978, Undersea Research Corporation fabricated the 1x64 beamformer printed circuit cards into a system and tested it in the laboratory. The purpose of these tests was to establish that the technology could be successfully applied to array configurations of more than 16 channels.

Section 2 discusses the derivation and operating characteristics of the analog FFT beamformer. Appendix A continues this discussion of the analog FFT derivation for large arrays. Appendix B gives a detailed derivation of the beamformer's beam ambiguity resolution circuits.

Section 3 discusses the derivation and operating characteristics of the beam focusing circuits.

Section 4 describes the particular hardware systems that have been built and their test results.

Section 5 compares the advantages and disadvantages of implementing the beamformer in advanced hardware technologies.

Section 6 discusses potential applications for this technology and Section 7 presents conclusions.

2. THE BEAMFORMER

2.1 INTRODUCTION

This section describes the analog FFT beamformer. It outlines the derivation of the discrete Fourier transform equations that were implemented in analog circuitry, describes these FFT circuits, and discusses some of their operational characteristics. It also outlines the derivation of equations to resolve the left-right beam ambiguity implicit in the Fourier coefficients and describes the implementation of these equations in hardware. Both the FFT circuits and the beam ambiguity resolving circuits are required for most beamformer applications.

Further detail on the derivation of the FFT card is given in Appendix A. The derivation of the beam ambiguity resolver is given in more detail in Appendix B.

In addition, this section discusses such beamformer operating characteristics as dynamic range, computation errors and data throughput rate of the beamformer.

2.2 THE ANALOG FFT

The one-dimensional discrete Fourier transform (DFT) is given by

$$X(k) = \sum_{n=0}^{N-1} x(n)\epsilon^{-j\frac{2\pi}{N}kn} \qquad k=0,1,\ldots,N-1 \qquad (2-1)$$

where for a beamformer

    $X(K)$ is the output beam k

    N is the number of hydrophones in the array

    n is the index for hydrophone n

    $x(n)$ is the time trace of the data received by hydrophone n.

Equation (2-1) can be written as

$$X(k) = \sum_{n=0}^{N-1} x(n)\cos\frac{2\pi}{N}kn \quad -j \sum_{n=0}^{N-1} x(n)\sin\frac{2\pi}{N}kn \qquad (2\text{-}2)$$

$$k=0,1,\ldots,N-1$$

It can be shown that if the input data $x(n)$ is real, only $\frac{N}{2}$ independent output beams will be formed. That is $X(i)$ will equal the complex conjugate of $X(N-1-i)$. This follows from the following properties of $\epsilon^{-j\frac{2\pi}{N}}$:

$$\epsilon^{-j\frac{2\pi}{N}k(N-n)} = \epsilon^{j\frac{2\pi}{N}kn} = \epsilon^{-j\frac{2\pi}{N}(N-k)n} \qquad (2\text{-}3)$$

$$\epsilon^{-j\frac{2\pi}{N}kn} = \epsilon^{-j\frac{2\pi}{N}k(n+N)} = \epsilon^{-j\frac{2\pi}{N}(k+N)n} \qquad (2\text{-}4)$$

This is the left-right beam ambiguity problem mentioned in Section 2.1.

Equation (2-2) could be implemented directly by summing the N hydrophone inputs $x(n)$ where each is weighted by the proper value of $\cos\frac{2\pi}{N}kn$. The sum of the same N hydrophone inputs weighted by $\sin\frac{2\pi}{N}kn$ could be formed, and both factors combined in a way that would result in N independent beams (as will be discussed later). An obvious implementation approach for both the real and the imaginary parts of Equation (2-2) would be to use an operational amplifier in a standard summation circuit as shown in Figure 2-1.

As N becomes larger than 4, the errors caused by the large number of inputs load the operational amplifier and a direct implementation of the sums in Equation (2-2) becomes impractical. As in the case of digital FFT algorithms that describe Equation (2-2) in a manner matched to the operational requirements of digital hardware, it is desirable to change the form of Equation (2-2) to match the type of

analog hardware implementation shown in Figure 2-1. An
obvious approach would be to derive the real and imaginary
parts of Equation (2-2) in the form of the summation of
summed terms where each sum contains no more than 4 elements.

If Equation (2-2) is considered for the case of only
16 inputs (N=16) it becomes

$$X(k) = \sum_{n=0}^{15} x(n)\cos\frac{\pi}{8}kn \quad -j \sum_{n=0}^{15} x(n)\sin\frac{\pi}{8}kn \qquad (2\text{-}5)$$

$$k=0,1,\ldots,N\text{-}1$$

For beam k=1 the value of cosine factors that multiply
the data received by each hydrophone (n) are shown in
Figure 2-2 beginning at 1 for n=0 and moving counterclockwise
around the circle for each succeeding value of n, that is

$$\sum_{n=0}^{15} x(n)\cos\frac{\pi}{8}n = x(0) + rx(1) + qx(2) + px(3) + \ldots \qquad (2\text{-}6)$$

For beam k=2, the cosine term begins at 1 for n=0 and takes
on every other value counterclockwise around Figure 2-2, that
is

$$\sum_{n=0}^{15} x(n)\cos\frac{\pi}{4}n = x(0) + qx(1) - qx(3) - x(4) - \ldots \qquad (2\text{-}7)$$

For beam k=i, x(0) is multiplied by 1 and each succeeding
value of x(n) is multiplied by the sample i places
counterclockwise from the previous one. The values for the
sine factors that multiply the data received by each
hydrophone (n) are obtained in the same manner for each beam

2-3
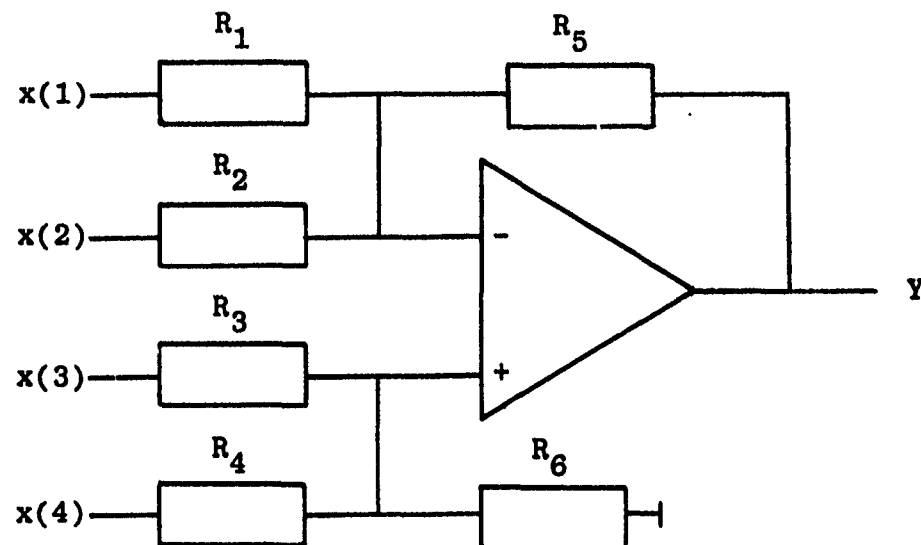
$$Y = -\frac{R_5}{R_1} x(1) - \frac{R_5}{R_2} x(2) + \frac{R_5}{R_3} x(3) + \frac{R_5}{R_4} x(4)$$

Figure 2-1. Typical operational amplifier summer with 4 inputs.
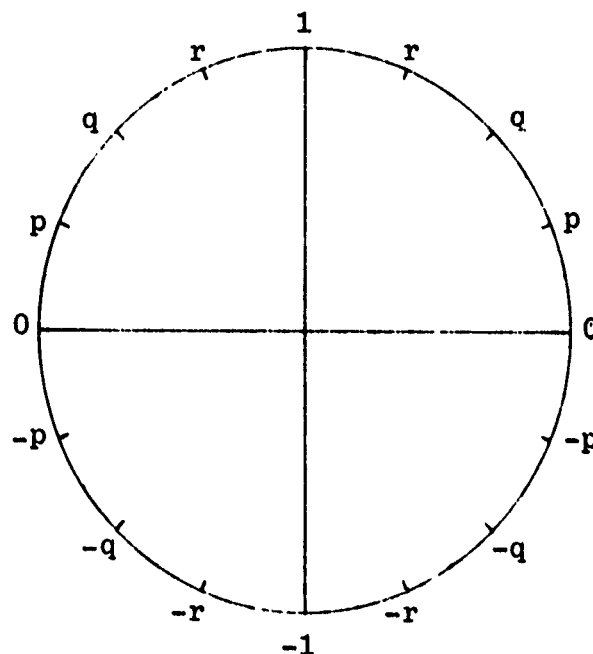
Figure 2-2. Determination of samples of the first 16 terms
of the discrete Fourier series. $p=\sin\pi/8$,
$q=\sin2\pi/8$, $r=\sin3\pi/8$, $1=\sin\pi/2$.

k except that the coefficient of x(0) is always 0 and the
multiplication factors begin at 0 (instead of 1) and move
counterclockwise around the circle. Figure 2-3 shows another
way of viewing this. This figure shows values of k only to
k=8, however as Equation (2-3) indicates, beams 9 through 15
are complex conjugates of beams 1 through 7 for the case of
real input data. Beam 0 is the broadside beam and beam 8 is
a beam whose sine component is zero for all samples.

A better view of the symmetry properties of Equation
(2-2) can be seen if Figure 2-3 is put in the matrix format
of Table 2-1, where x(n) represents the input data from
sensor n. If the proper inputs, x(n), are summed together to
take advantage of the symmetry of Equation (2-2), Table 2-1
can be simplified as shown in Table 2-2. Si is the value
sine multiplier in Equation (2-5) for the ith beam, and ci is
the value of the cosine multiplier.

Table 2-2 sums two input data channels together and
reduces the number of multiples required for each beam by a
factor of 2; there is no change in the number of additions
required. By taking advantage of the symmetry remaining in
Table 2-2, the number of multiples can again be cut in half
without changing the number of additions required, as shown
in Table 2-3. Each sum now contains four terms and can
easily be implemented by using the circuit shown in Figure
2-1. A circuit implementation is shown in Figure 2-4;
indices 16 through 47 are the same as those shown in Table
2-3. There is some symmetry in Table 2-3 that could be used
to further reduce the number of multiplications required,
however this would produce little additional advantage since
the same number of circuit components are required for
addition as for multiplication, and since the number of
inputs to e ch operational amplifier has been reduced to a
maximum of 4 in Figure 2-4.

If N is greater than 16 the same technique can be
employed to derive the Fourier transform circuits. In fact,
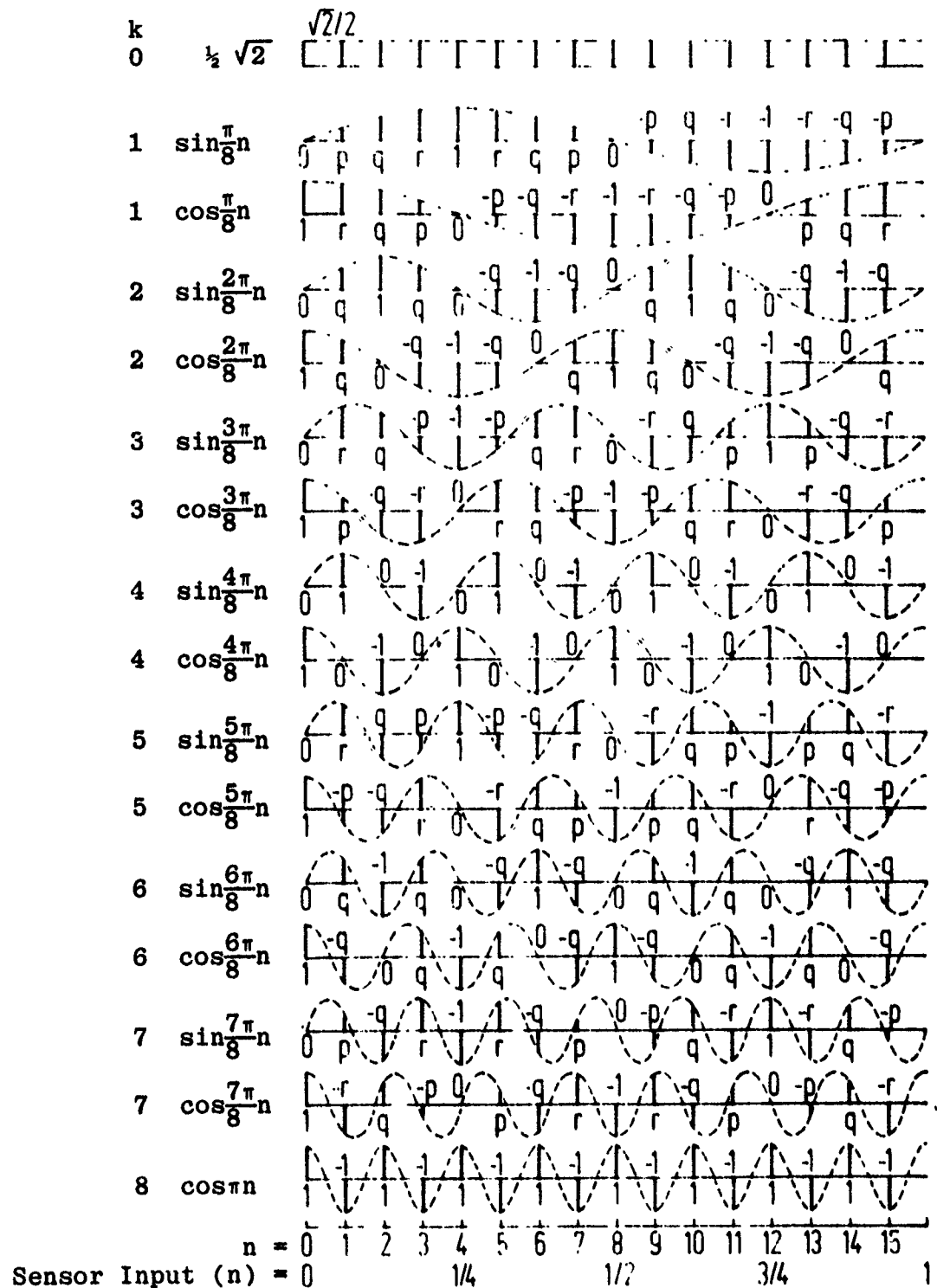
Figure 2-3. The first 16 functions of the discrete Fourier series as a function of k and n.

n	0	1	2	3	4	5	6	7	8	9	10	11	12	13	14	15
F(n)	A	B	C	D	E	F	G	H	I	J	K	L	M	N	O	P
0	q	q	q	q	q	q	q	q	q	q	q	q	q	q	q	q
s1	0	p	q	r	1	r	q	p	0	-p	-q	-r	-1	-r	-q	-p
c1	1	r	q	p	0	-p	-q	-r	-1	-r	-q	-p	0	p	q	r
s2	0	q	1	q	0	-q	-1	-q	0	q	1	q	0	-q	-1	-q
c2	1	q	0	-q	-1	-q	0	q	1	q	0	-q	-1	-q	0	q
s3	0	r	q	-p	-1	-p	q	r	0	-r	-q	p	1	p	-q	-r
c3	1	p	-q	-r	0	r	q	-p	-1	-p	q	r	0	-r	-q	p
s4	0	1	0	-1	0	1	0	-1	0	1	0	-1	0	1	0	-1
c4	1	0	-1	0	1	0	-1	0	1	0	-1	0	1	0	-1	0
s5	0	r	-q	-p	1	-p	-q	r	0	-r	q	p	-1	p	q	-r
c5	1	-p	-q	r	0	-r	q	p	-1	p	q	-r	0	r	-q	-p
s6	0	q	-1	q	0	-q	1	-q	0	q	-1	q	0	-q	1	-q
c6	1	-q	0	q	-1	q	0	-q	1	-q	0	q	-1	q	0	-q
s7	0	p	-q	r	-1	r	-q	p	0	-p	q	-r	1	-r	q	-p
c7	1	-r	q	-p	0	p	-q	r	-1	r	-q	p	0	-p	q	-r
c8	1	-1	1	-1	1	-1	1	-1	1	-1	1	-1	1	-1	1	-1

Table 2-1. The values of the samples of the 16 functions of the Fourier series in Figure 2-3. $p=\sin\pi/8$, $q=\sin\pi/4=\sqrt{2}/2$, $r=\sin3\pi/8$.

	A+I	B+J	C+K	D+L	E+M	F+N	G+O	H+P	A−I	B−J	C−K	D−L	E−M	F−N	G−O	H−P
0	q	q	q	q	q	q	q	q								
s1									0	p	q	r	1	r	q	p
c1									1	r	q	p	0	−p	−q	−r
s2	0	q	1	q	0	−q	−1	−q								
c2	1	q	0	−q	−1	−q	0	q								
s3									0	r	q	−p	−1	−p	q	r
c3									1	p	−q	−r	0	r′	q	−p
s4	0	1	0	−1	0	1	0	−1								
c4	1	0	−1	0	1	0	−1	0								
s5									0	r	−q	−p	1	−p	−q	r
c5									1	−p	−q	r	0	−r	q	p
s6	0	q	−1	q	0	−q	1	−q								
c6	1	−q	0	q	−1	q	0	−q								
s7									0	p	−q	r	−1	r	−q	p
c7									1	−r	q	−p	0	p	−q	r
c8	1	−1	1	−1	1	−1	1	−1								

Table 2-2. Sums and differences of the inputs A...P and the
values 0, $\pm p$, $\pm q$, $\pm r$, ± 1 of the samples of the
16 functions of the Fourier series by which they
are multiplied.

		16	17	18	19	20	21	22	23	24	25	26	27	28	29	30	31
		4 12 (E+M) 8 0 (A+I)	5 13 (F+N) 9 1 (B+J)	6 14 (G+O) 10 2 (C+K)	7 15 (H+P) 11 3 (D+L)	4 12 (E+M) 8 0 (A+I)	5 13 (F+N) 9 1 (B+J)	6 14 (G+O) 10 2 (C+K)	7 15 (H+P) 11 3 (D+L)	4 12 E−M 8 0	7 15 (H−P) 9 1 (B−J)	6 14 (G−O) 10 2 (C−K)	5 13 (F−N) 11 3 (D−L)	4 12 E−M 8 0 A−I	7 15 (H−P) 9 1 (B−J)	6 14 (G−O) 10 2 (C−K)	5 13 (F−N) 11 3 (D−L)
32	0	q	q	q	q												
40	s1									1	p	q	r				
44	c1													1	r	q	p
36	s2					0	q	1	q								
37	c2					1	q	0	−q								
41	s3									−1	r	q	−p				
45	c3													1	p	−q	−r
33	s4	0	1	0	−1												
34	c4	1	0	−1	0												
42	s5									1	r	−q	−p				
46	c5													1	−p	−q	r
38	s6					0	q	−1	q								
39	c6					1	−q	0	q								
43	s7									−1	p	−q	r				
47	c7													1	−r	q	−p
35	c8	1	−1	1	−1												

Table 2-3. Sums and differences of four samples A...P and the values 0, ±p, ±q, ±r, ±1 of the samples of the 16 functions of the Fourier series by which they are multiplied.

2-10
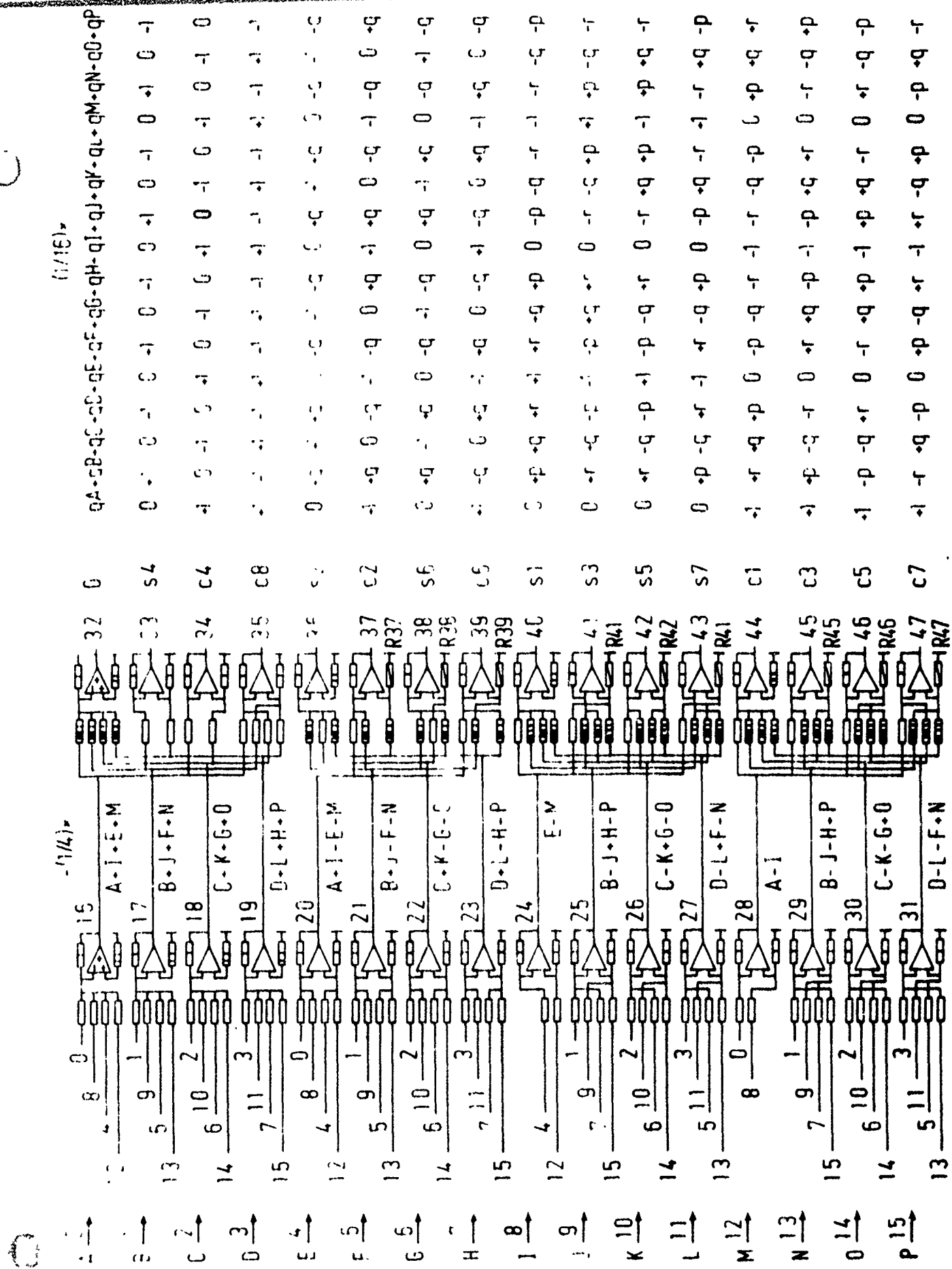
Figure 2-4.   16 channel analog FFT circuit.

like the digital FFT algorithms, this technique can be shown to work for any system with $2^k 3^m 5^n$ inputs, where $k,m,n=0,1,2....$ This is discussed further in Appendix A.

In the application of interest here — beamforming — each input, A,B,C,...,P, in Figure 2-4 is a channel of analog data, and each analog output, 32,33,34,...,47, is either a sine summation or a cosine summation for beam k in Equation (2-5). Since for most beamforming applications the input data is real, half of the output beams will be complex conjugates of the other half, only 7 sine and 7 cosine terms are required to define 14 beams, of which only 7 are independent. The broadside beam is also an independent beam. The eighth cosine term, for k=8 in Figure 2-3, will provide a beam that cannot be resolved between the left and right side of broadside.

2.3 BEAM AMBIGUITY RESOLUTION

It was shown in Section 2.2 that for N channels of real input data only $\frac{N}{2}$ independent output beams are obtained; beam k is the complex conjugate of beam (N-k), where k=0 is the broadside beam. If only the real portion of beam k is displayed (see Equation (2-2)) it will be identical to the real portion of beam (N-k). To differentiate between these two beams the imaginary portion of each beam must be incorporated into the displayed data. An obvious approach to solve this ambiguity would be to phase shift the imaginary term in Equation (2-2) by 90° and add it, with the appropriate sign, to the real term. As will be shown in Appendix B, this does produce unique output beams for the case of narrowband input signals.

An implementation of this beam ambiguity resolving approach using an operational amplifier integrator circuit is shown in Figure 2-5. Si and ci in Figure 2-5 are the output sine and cosine terms from the Fourier transform circuit of Figure 2-4.
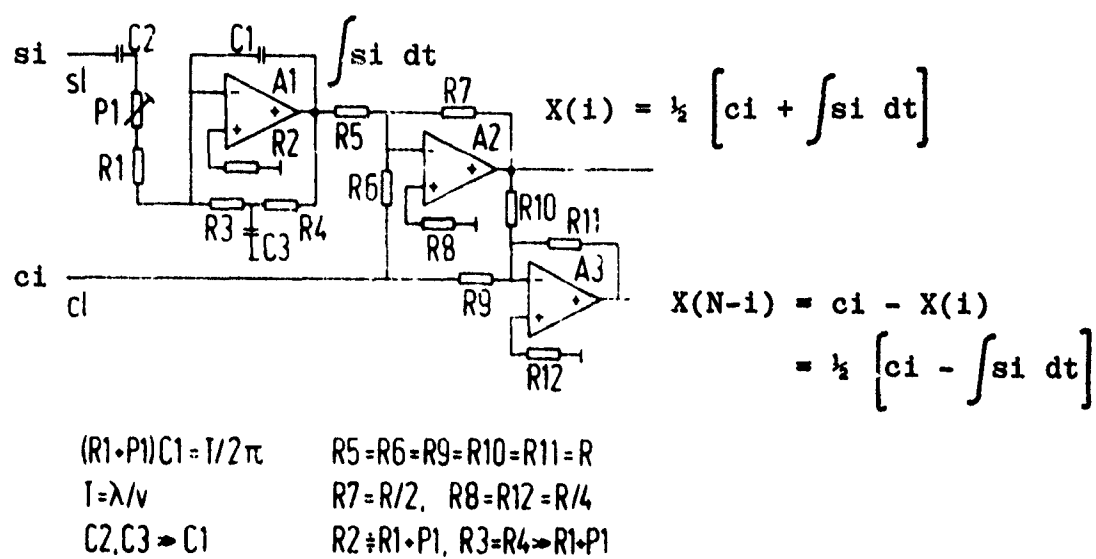
Figure 2-5. Beam ambiguity resolving circuit.

A complete beamformer with N analog input channels of data and N-1 unique analog beams out would require a circuit like that in Figure 2-5 for each sine and cosine output pair from the Fourier transform circuit. Figure 2-4 would require 7 such circuits producing two unique beams each. The output at indices 32 and 35 are the broadside beam which is unique and the endfire beam respectively.

The implementation of the beam ambiguity resolver circuit and the analog FFT circuit are similar. This could be an important consideration if sophisticated packaging techniques were being used, as will be discussed in Section 5.

2.4   BEAMFORMER OPERATING CHARACTERISTICS

The beamformer described by Figures 2-4 and 2-5 takes N channels of analog data in and outputs N-1 unique analog beams. Since the beam ambiguity circuit (Figure 2-5) uses an integrator to obtain a 90° phase shift of a sinusoid, the resulting beamformer is rather narrowband, however over the passband of the beamformer the beam pattern is identical to that of any Fourier transform beamformer with N inputs; the beam width and beam look direction are a function of the frequency of the input data.

The implementation of the Fourier transform equations in Table 2-3 is given by Figure 2-4. The constants multiplying the input to each operational amplifier can be simply approximated by the resistor ratio, as shown in Figure 2-1; this approximation assumes that the circuit's bias currents are small. Errors in the resistor values will result in errors in the factors 1,0,p,q, and r in Table 2-3. The effects of these errors are similar to the effects of filter coefficient quantization errors in a digital FFT circuit. The smaller the error tolerance on the resistors used, the smaller the filter coefficient errors will be and the lower the errors, or noise, in the output beams will be.

2-14

There has been considerable effort spent investigating the effects of digital FFT filter coefficient quantization errors. While there is no direct relationship between resistor tolerances, given in percentages, and digital filter word sizes, it is possible to obtain the errors in the summer output of Figure 2-1 due to the resistor tolerances. These errors can be compared to the filter output errors due to filter coefficient quantization errors. This will allow the error analyses of digital FFT's to be used as a bound on the expected output error for the type of analog FFT circuit shown in Figure 2-4.

Let $\hat{k} = \dfrac{r_1}{r_5}$ be one of the desired filter coefficients as shown in Figure 2-1. If the actual resistors have tolerances of $\pm\epsilon\%$ of their value and are uniformly distributed over that range of values, then the actual value of k implemented will be

$$k = \frac{(1 + S_1)r_1}{(1 + S_5)r_5} \qquad \text{where } \frac{-\epsilon}{100} \leq S_1, \ S_5 \leq \frac{-\epsilon}{100} \qquad (2-8)$$

The error in the implemented filter coefficient can be represented as

$$\hat{k} \pm \text{ERROR} = k \qquad (2-9)$$

The maximum k then becomes

$$k = \hat{k} + \text{LARGEST POSITIVE ERROR} = \left[\frac{1 + \epsilon}{1 - \epsilon}\right] \frac{r_1}{r_5}$$

$$= \left[\frac{1 + \epsilon}{1 - \epsilon}\right] \hat{k} \doteq \left[1 + 2\epsilon\right] \hat{k} \qquad \text{for small } \epsilon \qquad (2-10)$$

$$\text{LARGEST POSITIVE ERROR} = 2\epsilon\hat{k} \qquad (2-11)$$

The minimum k becomes

$$k = \hat{k} - \text{LARGEST NEGATIVE ERROR} = \left[\frac{1 - \epsilon}{1 + \epsilon}\right]\hat{k} \doteq \left[1 - 2\epsilon\right]\hat{k} \tag{2-12}$$

$$\text{LARGEST NEGATIVE ERROR} = 2\epsilon\hat{k} \tag{2-13}$$

A digital filter coefficient capable of representing k to within $\pm 2\epsilon\hat{k}$ would require at least b bits where

$$b = \log_2 \frac{1}{2\epsilon\hat{k}} \tag{2-14}$$

The minimum b will be obtained for the maximum $\hat{k}$, which for an FFT algorithm, will be $\hat{k}=1$. Therefore the minimum number of bits required to duplicate the errors expected in the circuit of Figure 2-1 is

$$b_{min} = \log_2 \frac{1}{2\epsilon} \tag{2-15}$$

For $\epsilon=10\%$, $2<b_{min}<3$ bits. For $\epsilon=5\%$, $3<b_{min}<4$ bits. For $\epsilon=1\%$, $5<b_{min}<6$ bits.

Weinstein [6,8] has investigated the effects of digital FFT coefficient quantization statistically, i.e., each coefficient was assumed to have a random jitter. Although the nature of coefficient quantization is inherently nonstatistical, he has experimentally shown the results to be roughly correct. His model for the ratio of the mean square output error (δ_E) to the mean square output signal is

$$\frac{\delta_E^2}{\left[\frac{1}{N}\sum_{n=0}^{N-1}|f(n)|^2\right]} = (\log_r N)(\text{Variance of the Coefficient}) \tag{2-16}$$

where N is the number of inputs and r is the radix of the algorithm used. Since for the analog FFT implementation of Figure 2-4, r=4, and for a digital FFT r=2, the reduced number of stages in the analog implementation should result in less error, for a given N.

Tufts, Hershey and Mosier [7] have simulated the effects of digital FFT coefficient quantization errors on the transform X(k) for various representations of the filter coefficients. They have determined the spurious sidelobes caused by the filter coefficient quantization as a function of N, the number of FFT inputs. For the worst case, $N \geq 64$ and sign-magnitude representation of the coefficients, the largest spurious sidelobe as a function of the number of magnitude bits is given in Table 2-4.

From Table 2-4, if 10% resistors are used to implement the analog FFT circuit, the beam pattern distortions caused by the resistor tolerance can be expected to be better than -23.6 dB below the mainlobe. If 1% resistors are used, the maximum error sidelobe will be better than -40 dB down. If the assumption that the only significant error in the analog FFT circuit is that caused by the resistor errors is correct, then Equation (2-15) and Table 2-4 give the maximum spurious sidelobe expected for an analog FFT circuit. This is because the derivation above is done for the worst case of ϵ and k. In addition, Table 2-4 is based on a radix 2 system that will have $\log_2 \lceil N \rceil$ stages of multiplication, where N is the number of inputs. The analog FFT with 4 inputs per operational amplifier requires only $\log_4 \lceil N \rceil$ stages of multiplication, resulting in less output beam error than shown in Table 2-4; Equation (2-15) indicates half the error.

Figure 2-6 shows the theoretical broadside beam pattern for a line array of 64 equally-spaced hydrophones with no data weighting. The hydrophone spacing is assumed to be half of the input signal wavelength. Also shown on this figure as horizontal lines are the largest sidelobes as a

Number of Magnitude Bits H	Power Level of Largest Sidelobe (dB)
0	-12.0
1	-15.3
2	-23.6
3	-29.1
4	-36.6
5	-41.8
6	-46.3
7	-51.4
8	-60.4
9	-65.0
10	-71.0
11	-77.0
12	-83.4
13	-89.7
14	-95.6
15	-99.7

Table 2-4. Spurious sidelobe levels for different degrees
of FFT coefficient quantization.
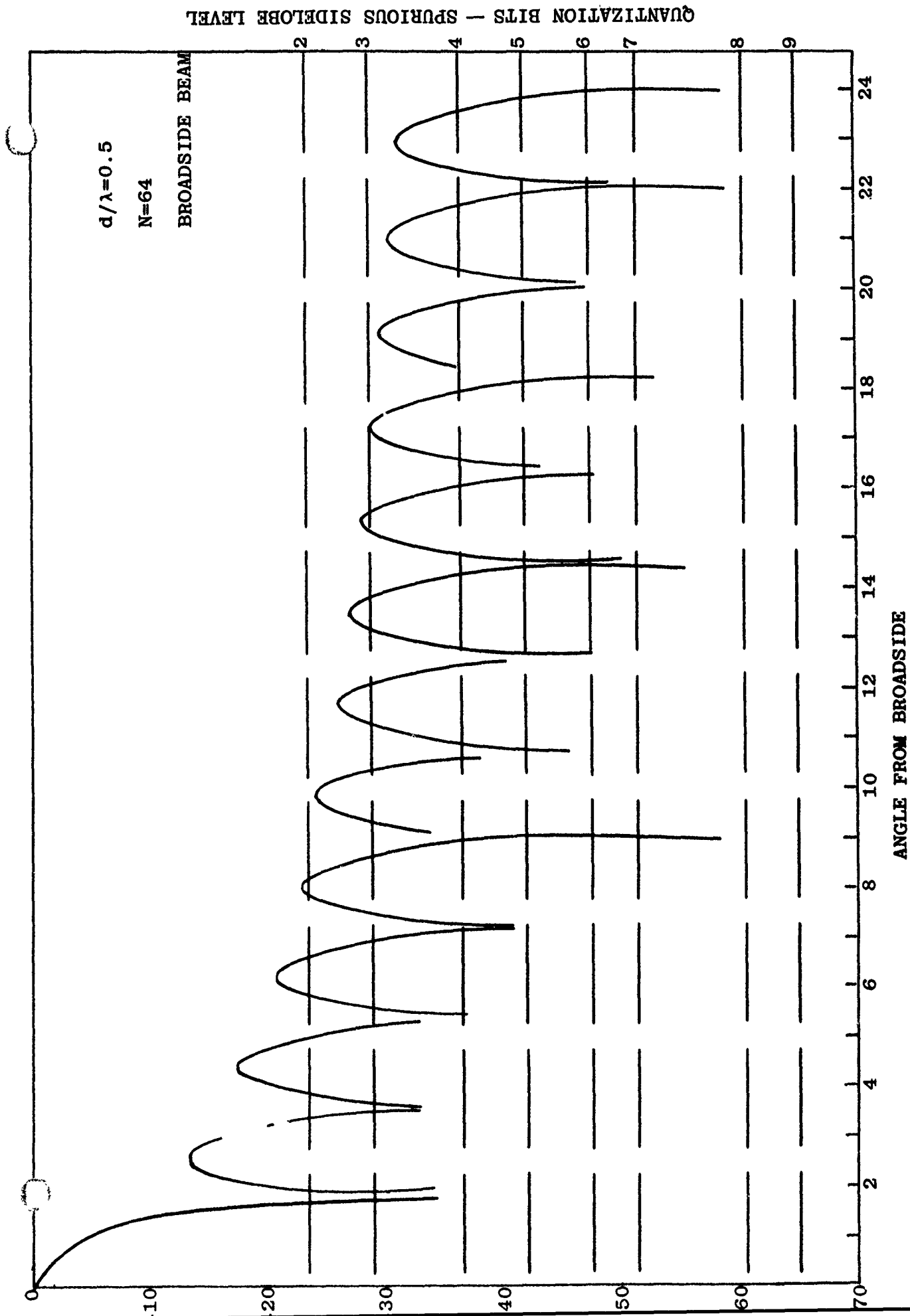
Figure 2-6. Beam pattern for a line array of 64 equally-spaced sensors. The largest spurious sidelobe level due to filter coefficient quantization according to

function of the number of bits used to represent the FFT filter coefficients taken from Table 2-4. Figure 2-7 shows the same data except that only the peak of each sidelobe is plotted. As can be seen, if a 64 input analog FFT beamformer uses 10% resistors, the peak spurious error sidelobe will be about equal to the fifth sidelobe from broadside and will be equivalent to a digital system using between 2 and 3 bits to represent the filter coefficients if the input data has no quantization error. If 1% resistors are used, the peak spurious sidelobe will be about 7 dB below the smallest theoretical sidelobe shown and equivalent to between 5 and 6 bits for filter quantization. If the more sophisticated packaging techniques discussed in Section 5 are used, resistor tolerances of 0.1% and better are well within the state of the art. This is equivalent to using 8 bit filter coefficient words and results in spurious sidelobes that are better than 25 dB below the smallest sidelobe in Figure 2-7. Since the input data is not quantized, the output data will have significantly less error than a digital filter using 8 bit filter coefficient.

2.5 THE TWO-DIMENSIONAL ANALOG FFT

The discrete Fourier transform in two dimensions is given by

$$X(k_1,k_2) = \sum_{n_1=0}^{N_1-1} \sum_{n_2=0}^{N_2-1} X(n_1,n_2) \, \varepsilon^{-j\left(\frac{2\pi}{N_1}\right)n_1 k_1} \, \varepsilon^{-j\left(\frac{2\pi}{N_2}\right)n_2 k_2}$$

(2-17)

$$k_1 = 0, 1, \ldots, N_1-1$$
$$k_2 = 0, 1, \ldots, N_2-1$$
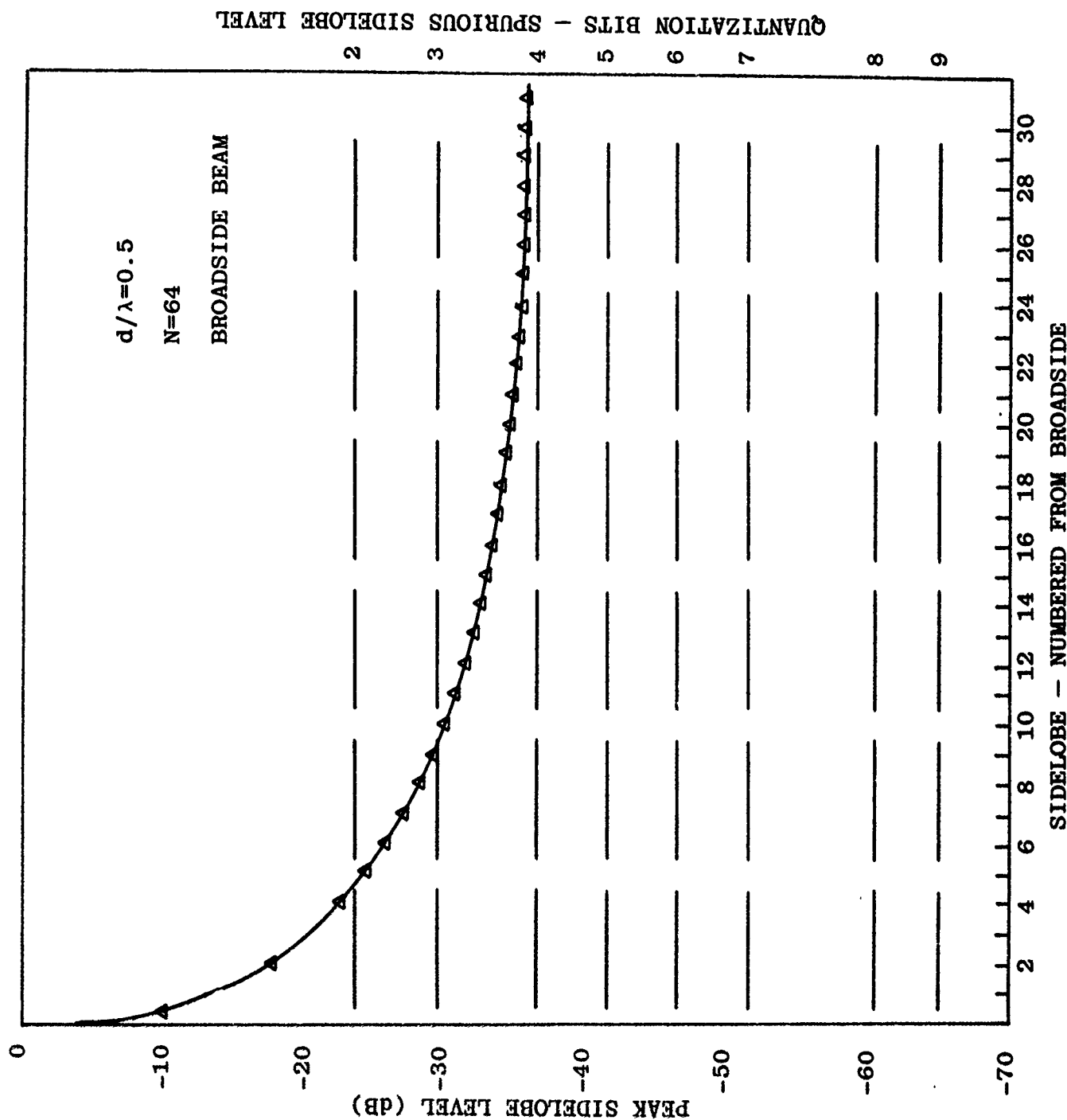
Figure 2-7. The peak sidelobe level for a line array of equally-spaced sensors. The largest spurious sidelobe level due to filter coefficient quantization according to Tufts, Hershey and Mosier is shown at the right.

$$X(k_1,k_2) = \sum_{n_1=0}^{N_1-1} \epsilon^{-j\left(\frac{2\pi}{N_1}\right)n_1 k_1} \left[\sum_{n_2=0}^{N_2-1} X(n_1,n_2)\, \epsilon^{-j\left(\frac{2\pi}{N_2}\right)n_2 k_2}\right]$$

(2-18)

Equation (2-18) shows that the two-dimensional analog FFT can be implemented one dimension at a time as shown in Figure 2-8. Each plane in Figure 2-8 represents a 1xN analog FFT circuit, such as shown in Figure 2-4. The rows of inputs from the receiving array are first transformed in the X-direction. The resulting transformed outputs are inputs to the Y-direction transforms, also implemented by circuits as shown in Figure 2-4.

As will be discussed in Section 4, a 16x16 array of hydrophones and a 16x16 analog FFT circuit have been built and tested as an acoustic imaging system. Such a system is shown in Figure 2-9. The sound projector illuminates the object plane. The 16x16 array of hydrophones receives the sound pressure that is scattered from the object plane and turns it into $16^2 \approx 256$ electrical signals. Sixteen printed circuit cards similar to the circuit shown in Figure 2-4 transform the data in the X-direction. Sixteen additional cards transform that data in the Y-direction, resulting in 16x16 points in the object plane being resolved for display. Since the data throughput rate of the analog circuits is very high, the potential for television-like moving images exists with this technology.
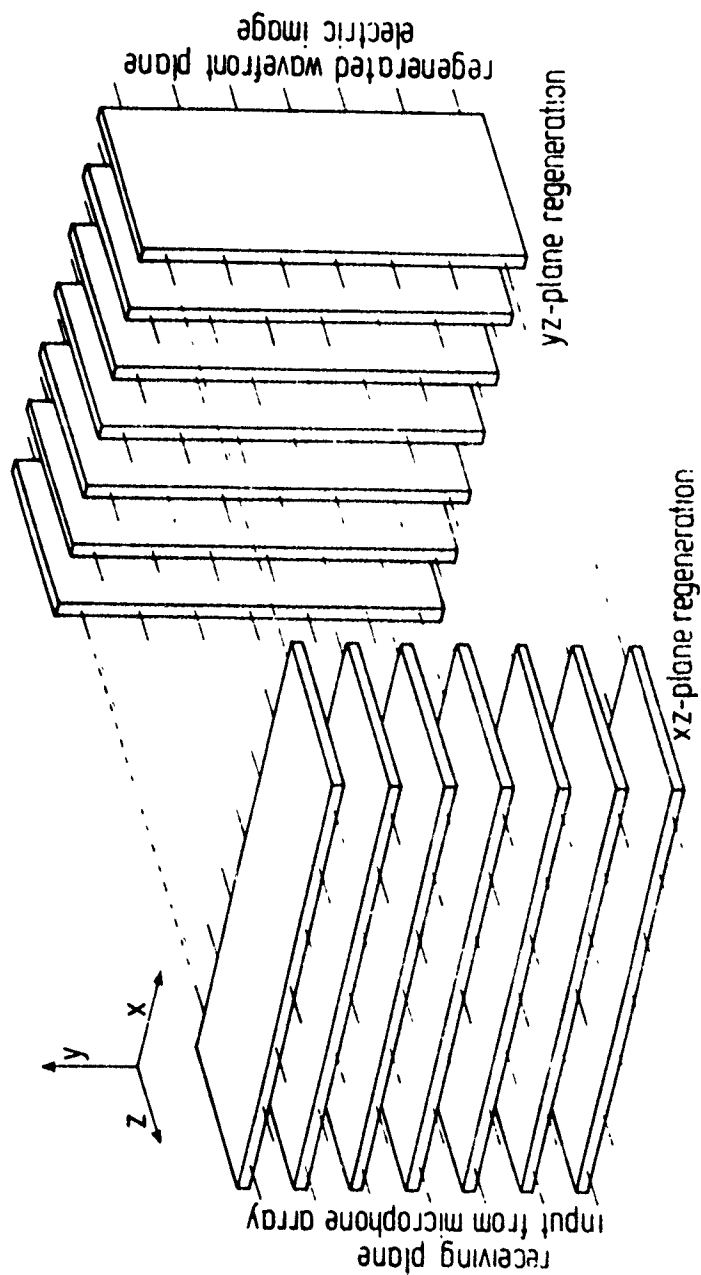
Figure 2-8. Two-dimensional analog FFT system transforming first in the X-direction and then in the Y-direction.
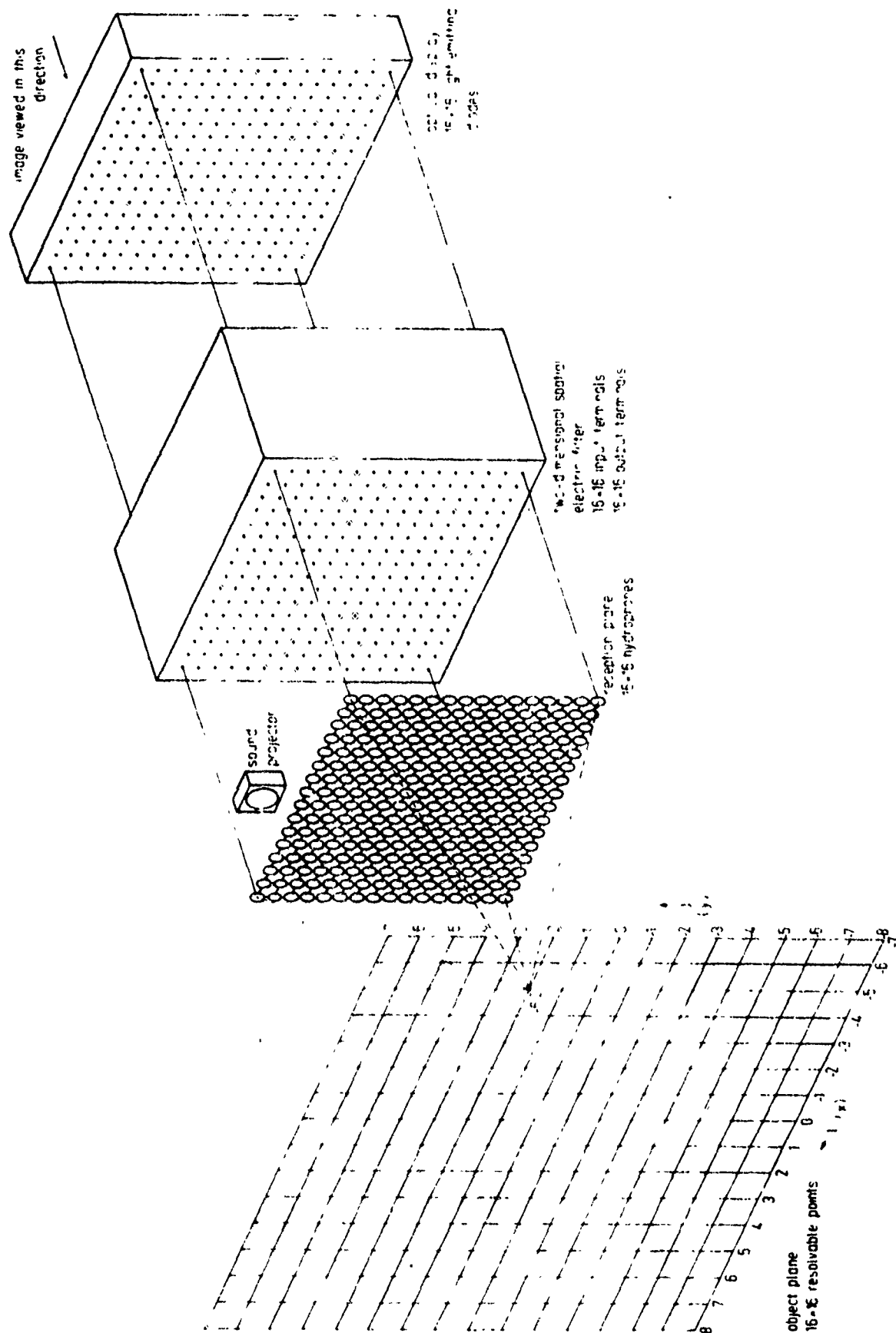
Figure 2-9. A two-dimensional acoustic imaging system using the analog FFT.

3. FOCUSING

3.1 INTRODUCTION

This section discusses pre-beamforming electronic filtering of signals from close sources received by an array that makes the data approximate plane waves. Most beamformers, including the one discussed in Section 2, assume the received signal will be a plane wave. Deviations from these assumptions cause errors in the output beams. Pre-filtering the wave to straighten its spherical shape across the array removes the output errors. This process can also be viewed as focusing the beamformer on a close source. As with focusing optical systems, a priori knowledge of the distance to the source is desirable.

The focusing technique discussed here will be for narrowband input signals, and will phase-weight the input data on each sensor to compensate for its phase relative to a reference input channel. Such circuits have been built and laboratory tested on the 64 input beamformer system.

Section 3.2 derives the focusing equations in one-dimension and briefly discusses the two-dimensional case.

Section 3.3 investigates the errors caused by being out of focus.

3.2 ELECTRONIC FOCUSING

This section will first derive the sensor-to-sensor input signal phase differences from a close narrowband source in one-dimension. It will then illustrate a processing technique to eliminate these phase differences and make this input signal look like a plane wave and will discuss an implementation of this processor. Finally, focusing in two-dimensions will be discussed.

Consider the one-dimensional array of Figure 3-1. The distance between the plane of focus and the hydrophone array equals R. The point W_β on the plane of focus has the distance

ARRAY

7d/2
5d/2
3d/2
d/2
0
-d/2
-3d/2
-5d/2
-7d/2

$\dfrac{d_i}{2}$ for i odd

$R\left\{1 + \left(\tan\beta - \dfrac{d_i}{2R}\right)^2\right\}^{1/2}$

$R\left(1 + \tan^2\beta\right)^{1/2}$

R

β

R Tan β

WB
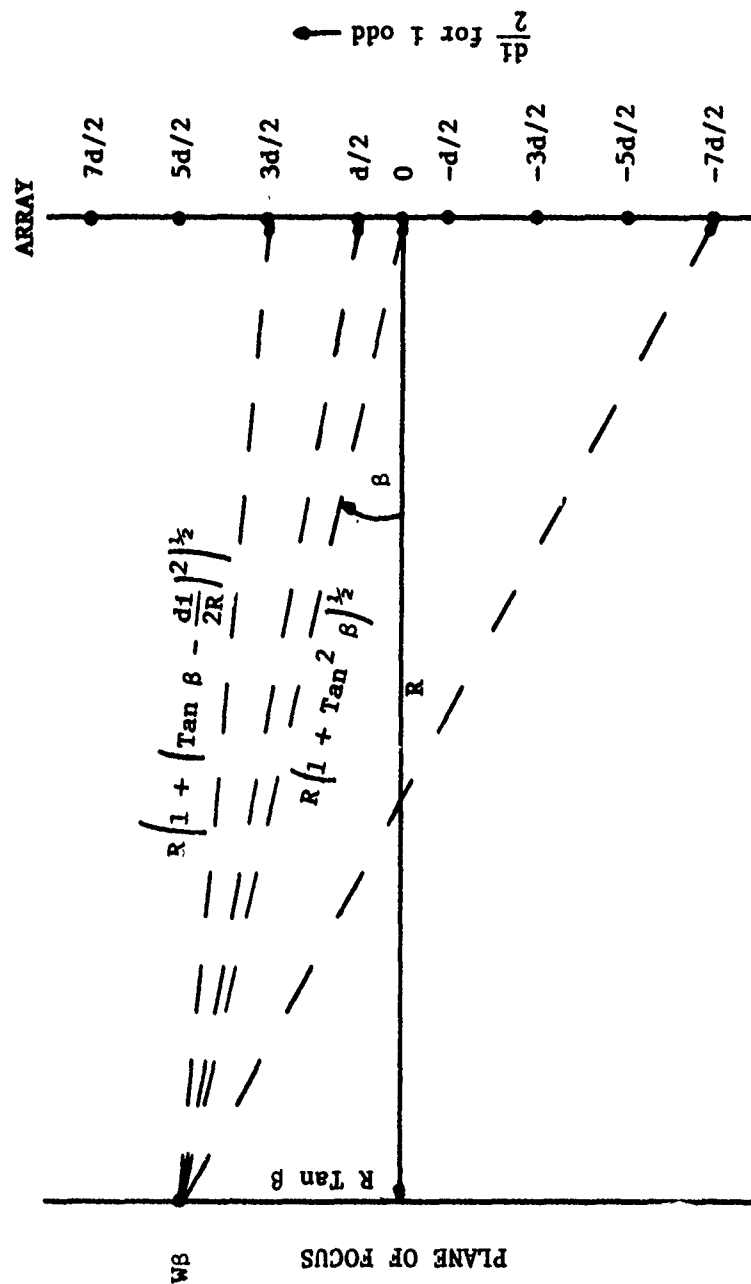
PLANE OF FOCUS

Figure 3-1. The derivation of the distance from a point WB in the plane of focus to points on a line array. The point 0 indicates the center of the array where the array has an odd number of hydrophones.

$$(R^2 + R^2\tan^2\beta)^{\frac{1}{2}} = R(1 + \tan^2\beta)^{\frac{1}{2}} \qquad (3\text{-}1)$$

from the center of the array. The distance between the point $W\beta$ and an arbitrary hydrophone i is defined by the relation

$$\left[R^2 + \left(R\tan\beta - \frac{di}{2}\right)^2\right]^{\frac{1}{2}} = R\left[1 + \left(\tan\beta - \frac{di}{2R}\right)^2\right]^{\frac{1}{2}}$$

for i odd $\qquad (3\text{-}2)$

The difference of the distances of Equations (3-1) and (3-2) multiplied by $\frac{2\pi}{\lambda}$ is called the relative phase $\psi(iR\beta)$:

$$\psi(iR\beta) = \frac{2\pi R}{\lambda}\left\{\left[1 + \left(\tan\beta - \frac{di}{2R}\right)^2\right]^{\frac{1}{2}} - \left(1 + \tan^2\beta\right)^{\frac{1}{2}}\right\}$$

for i odd $\qquad (3\text{-}3)$

$$\psi(iR\beta) = \frac{2\pi R}{\lambda}\left\{\left[\sec^2\beta - \frac{di}{R}\tan\beta + \frac{d^2i^2}{4R^2}\right]^{\frac{1}{2}} + \sec\beta\right\}$$

for i odd $\qquad (3\text{-}4)$

For small values of β one may replace $\sec\beta$ by 1, and $\tan\beta$ by $\sin\beta$ giving

$$\psi(iR\beta) \doteq \frac{2\pi R}{\lambda}\left\{\left[1 - \frac{di}{R}\sin\beta + \frac{d^2i^2}{4R^2}\right]^{\frac{1}{2}} - 1\right\} \quad \text{for i odd} \quad (3\text{-}5)$$

If, in addition, $\frac{di}{2R}$ is small for all values of i, then the square root term in Equation (3-5) may be approximated as

$$\left[1 - \frac{di}{R}\sin\beta + \frac{d^2i^2}{4R^2}\right]^{\frac{1}{2}} \doteq 1 - \frac{di}{2R}\sin\beta + \frac{d^2i^2}{8R^2} \qquad (3\text{-}6)$$

3-3

giving

$$\psi(iR\beta) \doteq \frac{2\pi R}{\lambda} \left\{ -\frac{di}{2R} \sin \beta + \frac{d^2 i^2}{8R^2} \right\} \qquad \text{for i odd} \quad (3\text{-}7)$$

As will be seen in Section 3.3, this approximation is valid for most cases of interest and will be considered throughout the remainder of this section.

Assuming a narrowband source $v(t)$,

$$v(t) = V \sin wt \qquad (3\text{-}8)$$

the output voltage of hydrophone i in Figure 3-1 is denoted $v(iR\beta t)$, where

$$v(iR\beta t) = V \sin \left[wt - \psi(iR\beta) \right] \qquad (3\text{-}9)$$

Using the approximation of Equation (3-7) one obtains the following output voltages:

$$v(iR\beta t) = V \sin \left[wt + \frac{\pi di}{\lambda} \sin \beta - \frac{\pi d^2 i^2}{4\lambda R} \right] \qquad (3\text{-}10)$$

$$\text{for i odd}$$

Equation (3-10) can be rewritten as

$$v(iR\beta t) = V \left[\sin \left(wt + \frac{\pi dR}{\lambda} \sin \beta \right) \cos \theta \right.$$
$$\left. + \cos \left(wt + \frac{\pi di}{\lambda} \sin \beta \right) \sin \theta \right] \qquad (3\text{-}11)$$

where i is odd and

$$\theta = \frac{\pi d^2 i^2}{4\lambda R} \qquad (3\text{-}12)$$

and Equation (3-11) is the voltage at the output of hydrophone i. The desired voltage into the beamformer on channel i is the voltage from a plane wave, i.e. R→∞, or,

$$v_D(iR\beta t) = V \sin\left[wt + \frac{\pi di}{\lambda} \sin \beta\right] \qquad \text{for i odd} \quad (3\text{-}13)$$

A rather straightforward approach to processing Equation (3-11) so that the result is Equation (3-13) is given by Equation (3-14).

$$v_D(iR\beta t) - v(iR\beta t) \cos \theta + v*(iR\beta t) \sin \theta \qquad (3\text{-}14)$$

where

$$v*(iR\beta t) = \frac{1}{W} \int v(iR\beta t) \, dt \qquad (3\text{-}15)$$

One of the major advantages to the techniques described by Equation (3-14) is that it can be implemented in hardware that is compatible with the analog FFT beamformer described in Section 2.

Equation (3-14) requires the multiplication of two time variable voltages $v*(iR\beta t)$ and $v(iR\beta t)$ with two constants, $\sin \frac{\pi d^2 i^2}{4R}$ and $\cos \frac{\pi d^2 i^2}{4R}$. The constants have to be computed every time a new focusing distance R is required. This computation is most readily done by a microprocessor, and the constants are then available as binary numbers. Hence, we need a multiplier that can multiply a rapidly varying voltage with a binary number.

Commercially available digital-to-analog converters can provide this capability. An implementation of Equation (3-14) is shown in Figure 3-2. Since i^2 appears in θ, the multiplication terms $\sin \theta$ and $\cos \theta$ will be the same for hydrophones at +i and -i and these circuits may be combined to save components.

In Figure 3-2, the operational amplifier circuits containing A11 and A21 are integrators and implement Equation (3-15). The circuits containing A12,A22,A31 and A32 are used to bias the zero mean AC input signal about a positive mean voltage, i.e. the output of these circuits is always positive. The DAC's and the associated circuitry containing A41,A42,A51 and A52 provide four two-quadrant multipliers that implement Equation (3-14). Digital numbers representing the values of $\sin \theta$ and $\cos \theta$ are serially shifted into SRr1 and SRr2 respectively. These values are then fed into the DAC's for multiplying the signals $v*(iR\beta t)$, $v*(-iR\beta t)$ and $v(-iR\beta t)$ respectively. The summation in Equation (3-14) is provided by the circuit containing A51 for $v_D(iR\beta t)$ and A61 for $v_D(-iR\beta t)$.

Electronic focusing in two-dimensions is a direct generalization of focusing in one-dimension. The arriving wavefronts are spherical and a square array will be assumed as shown in Figure 3-3. The 16x16 hydrophones in Figure 3-3 are numbered from the center of the array. The circles connect the hydrophones that are the same distance from the center of the array. If a source is assumed at an angle β_X from the center of the array in the X-direction and β_Y from the center of the array in the Y-direction, then by using the same small angle (β_X and β_Y) assumptions as were used to obtain Equation (3-5), and the assumption that the array aperture is small compared to the distance to the source, i.e. Equation (3-6), then the relative phase difference between a signal arriving at the center of the array and at hydrophone s,p can be shown to be

$$\psi(spR\beta_X\beta_Y) = \frac{2\pi}{\lambda} \left\{ -\frac{ds}{2} \sin \beta_X - \frac{dp}{2} \sin \beta_Y + \frac{d^2s^2}{8R} + \frac{d^2p^2}{8R} \right\}$$

for s,p odd (3-16)

3-6
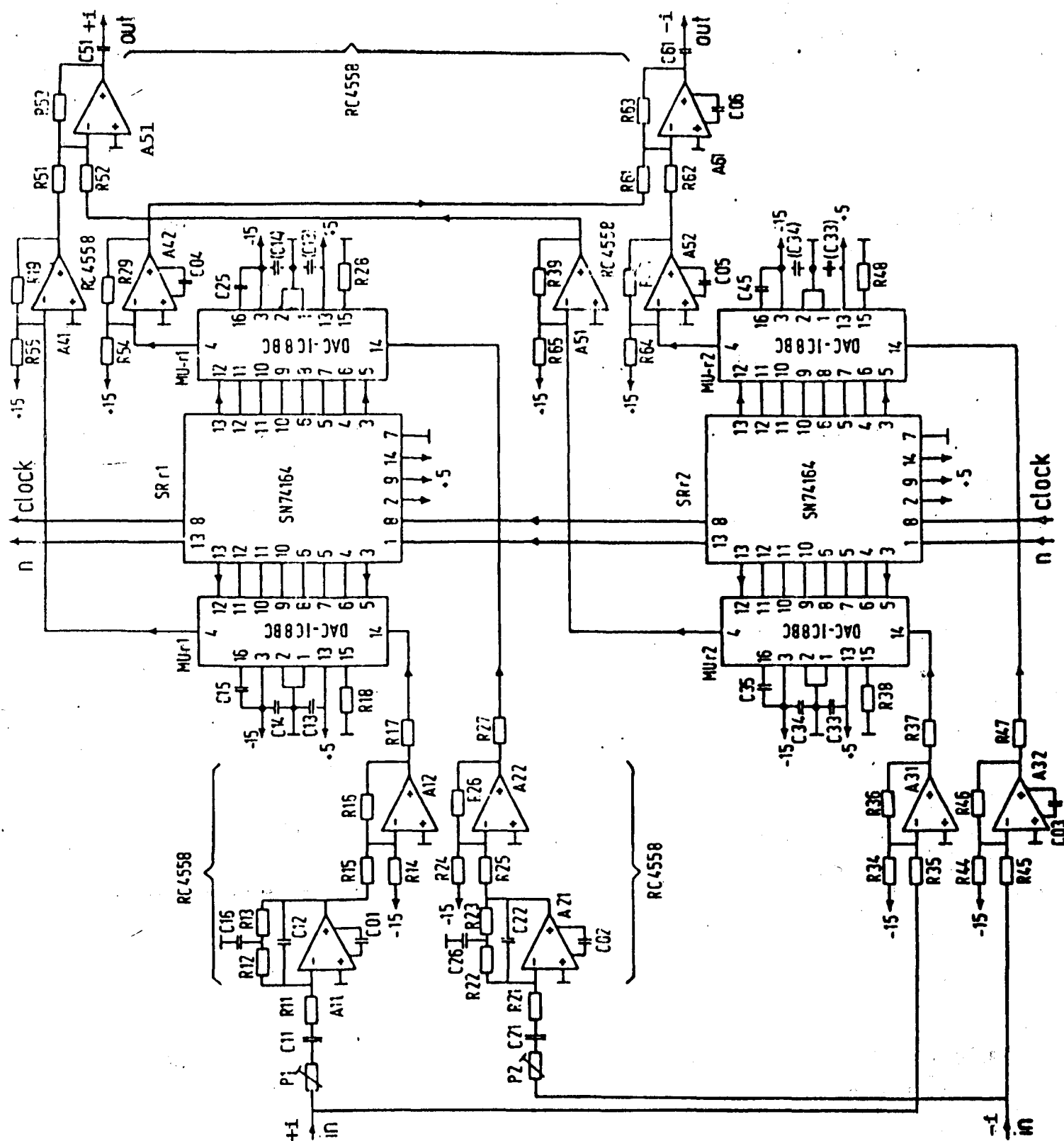
Figure 3-2. Focusing circuit for pairs of input voltages
$v(pR\beta t)$ and $v(-pR\beta t)$ that require multiplication
by the same constants $v_s(s,p)$ and $v_c(s,p)$.
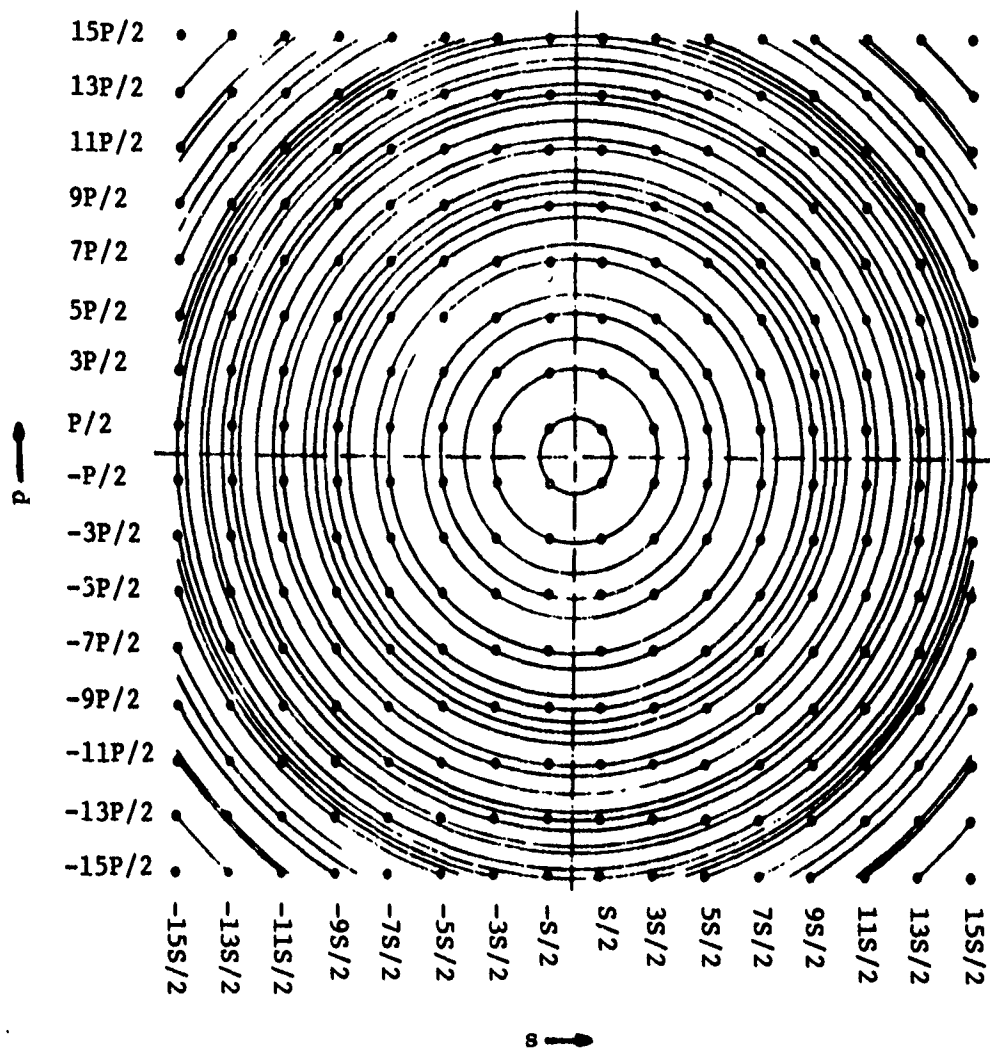
Figure 3-3.   Two-dimensional array of 16x16 hydrophones.
The hydrophones with equal distance from the
center of the array are connected by circles.

The two-dimensional hydrophone output voltages become

$$v(spR\beta_X\beta_Y t) = V \sin \left\{ wt - \psi(spR\beta_X\beta_Y) \right\} \quad \text{for s,p odd} \quad (3\text{-}17)$$

$$= V \sin \left\{ wt + \frac{\pi d}{\lambda} s \sin \beta_X + \frac{\pi d}{\lambda} p \sin \beta_Y \right.$$
$$\left. - \frac{\pi d^2}{4\lambda R} (s^2 + p^2) \right\} \quad \text{for s,p odd} \quad (3\text{-}18)$$

$$= V \sin \left\{ wt + \frac{\pi d}{\lambda} (s \sin \beta_X + p \sin \beta_Y) \right\} \cos \theta$$
$$- V \cos \left\{ wt + \frac{\pi d}{\lambda} (s \sin \beta_X + p \sin \beta_Y) \right\} \sin \theta$$
$$(3\text{-}19)$$

where s and p are odd and

$$\theta = \frac{\pi d^2}{4\lambda R} (s^2 + p^2) \quad (3\text{-}20)$$

The desired output voltage $V_D(spR\beta_X\beta_Y)$ is given by

$$V_D(spR\beta_X\beta_Y t) = v(spR\beta_X\beta_Y t) \cos + v^*(spR\beta_X\beta_Y t) \sin \quad (3\text{-}21)$$

where

$$v^*(spR\beta_X\beta_Y t) = \frac{1}{W} \int v(spR\beta_X\beta_Y t) \, dt \quad (3\text{-}22)$$

The circuit of Figure 3-2 with Equation (3-20) substituted into the cos θ and sin θ terms will provide focusing in two-dimensions.

3.3   OPERATING CHARACTERISTICS

This section discusses errors in the beam pattern that result from errors in focusing.

The circuits derived in Section 3.2 are based on the approximation for the relative phase, $\psi(iR\beta)$, given by Equation (3-7). This approximation assumed that the source was close to the broadside direction, β is small, and many array apertures away, the maximum $\frac{id}{R} = \frac{A}{R}$ is small. If both assumptions are true, the derived focusing system will produce satisfactory results. Figure 3-4 shows the required target range as a function of the array aperture in wavelengths for a maximum phase error of $\lambda/8$. If β is in fact not small ($\beta=45^{\circ}$), then the target range and the array aperture parameters must fall into the unshaded region to the left in Figure 3-4 for a $\lambda/8$ phase error tolerance to be maintained. If β is small ($\beta<10^{\circ}$), then the target range and array aperture parameters must fall to the left of the doubly shaded region of Figure 3-4 for the phase error tolerance of $\lambda/8$ to be maintained.

The remainder of this section considers the case where Equation (3-7) is valid, but where the target does not reside in the plane of focus, i.e. R is incorrectly known.

Figure 3-5 shows the broadside beam for a square array of 16x16 hydrophones and an aperture A that is 15 times the closest neighbor hydrophone distance, A=15d. The distance R to the target equals 10A and the target is at broadside. The diffraction pattern is not circularly symmetric since the hydrophone array is a Cartesian array.[1]

The excellent diffraction pattern of Figure 3-5 degenerates rapdily if the object is not at the focusing distance R but at another distance R_0. The resulting diffraction patterns are shown for R_0 = 14A,10A,8A and 7A in Figure 3-6. The pattern is not only widened but its center may become smaller than other sections of the pattern if the focusing distance R differs from the actual distance R_0. For

---

[2] The computer plots of this section were obtained by Mohamed (1976) through simulation of the sound waves.
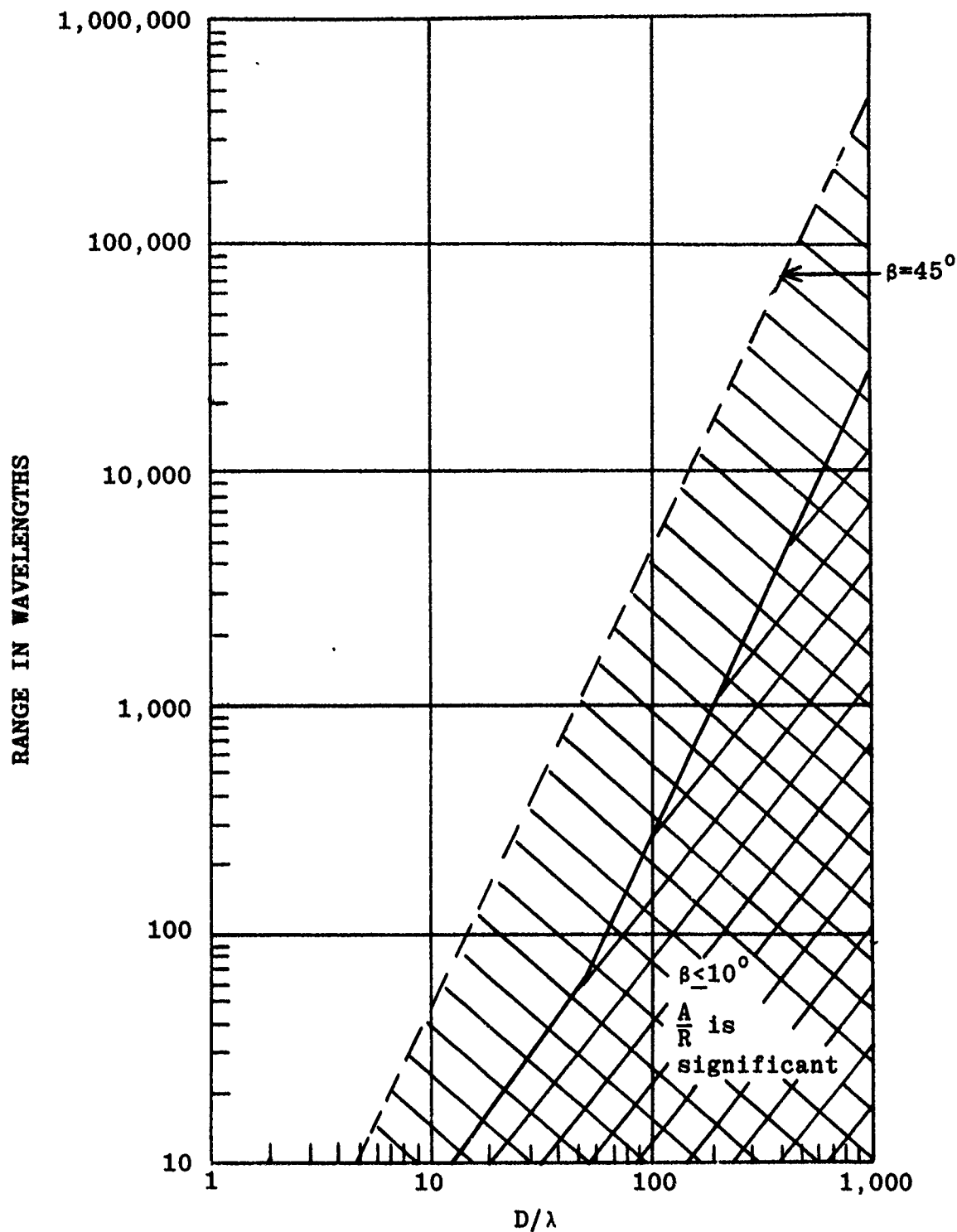
Figure 3-4.   Target and array parameters required for a
             maximum phase error tolerance of $\lambda/8$.   (After
             D. H. Brown, Naval Ship Research and Development
             Laboratory, Panama City, Florida.)
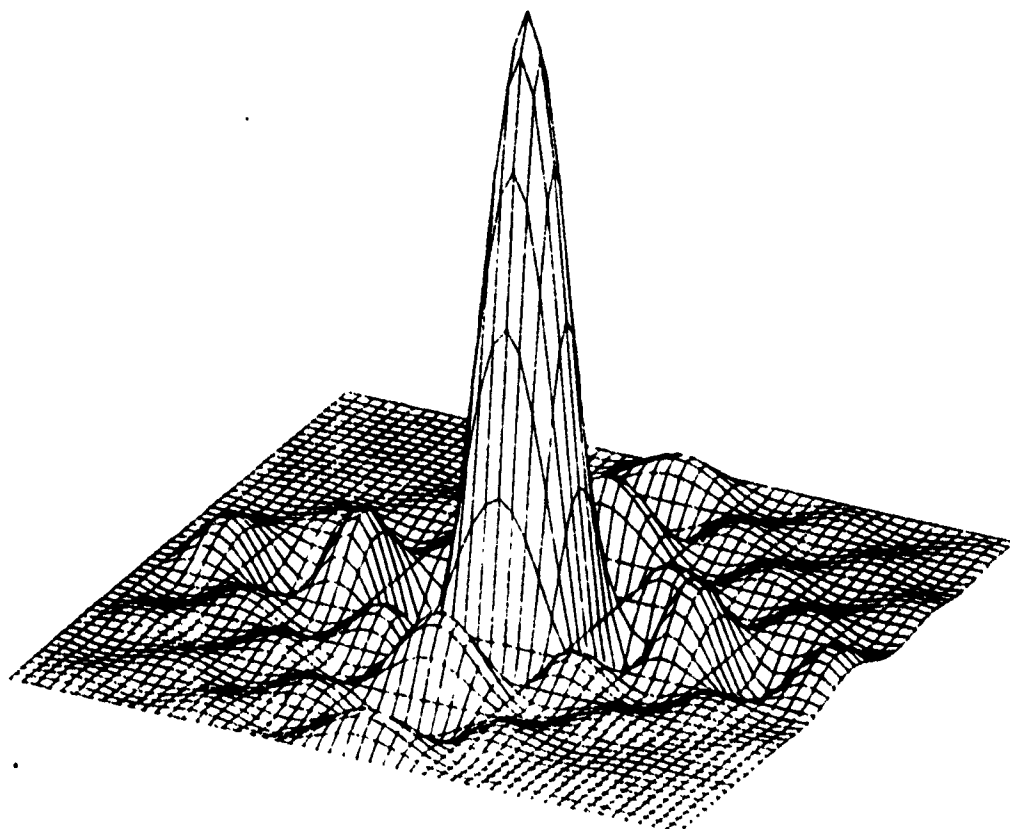
Figure 3-5. Diffraction pattern $v(R, \gamma_x, \gamma_y, \gamma_x, \gamma_y)$ for R=10A, $\gamma_x = \gamma_y = 0$ of a hydrophone array with 16x16 hydrophones and an aperture A=15d. (Courtesy N. Mohamed, Government of Kuwait.)

instance, the image of the poorly focused point at broadside in Figure 3-6 looks like a properly focused image of four adjacent points.

Some of the asymmetries in Figure 3-6 are due to the small number of 16x16 hydrophones, since an array with an even number of hydrophones is inherently asymmetric if one wants to form the broadside beam. This type of asymmetry decreases with an increasing number of hydrophones. Hence, diffraction patterns for an array with 64x64 hydrophones are shown in Figure 3-7. The focusing distance equals R=5A while the imaged point is actually at the distance $R_0 = 6.5A, 6A, 4.5A$ or $4A$.

The comparison of Figures 3-6 and 3-7 shows that the reduction of the realtive focusing distance R/A from 10 to 5 makes the patterns more sensitive to an incorrect distance R. This sensitivity is well-known in photography as the reduction of the depth of field with decreasing distance of the object.

The depth of field is generally defined as the deviation of the object distance R_0 from the focusing distance R that can be tolerated without making the image of a point at R_0 appear objectionably blurred. The more specific definition varies according to the intended use. In optics one generally uses a definition based on geometric optics. The image of a point out-of-focus is a circular disc according to geometric optics. The image of the same point in focus yields a diffraction pattern (or beam pattern in acoustics) according to wave optics. The point is within the depth of field if the radius of the disc is no larger than the distance of the first zero corssing of the diffraction pattern from its center. This definition is not suited for acoustic beamforming. However, it defines the depth of field essentially by requiring that the beam pattern of the out-of-focus image should not be more than twice as wide as the beam pattern of the focused image. This definition is usable in acoustic beamforming.
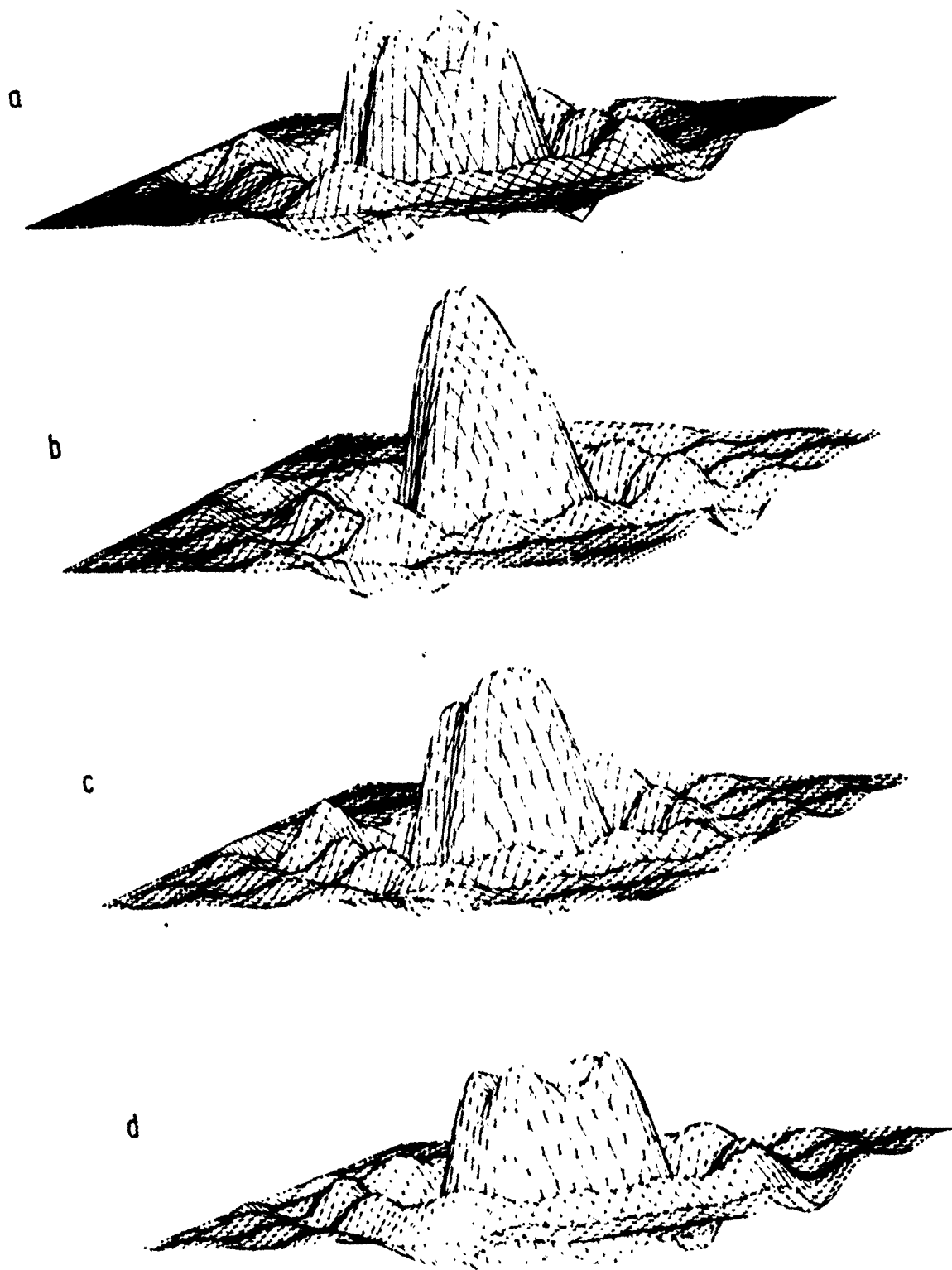
Figure 3-6. Diffraction patterns according to Figure 3-5 but with the imaged point at the actual distance R_0 instead of the focusing distance $R=10A=150d$. (a) $R_0=14A$, (b) $R_0=13A$, (c) $R_0=8A$, (d) $R_0=7A$. (Courtesy N. Mohamed, Government of Kuwait.)
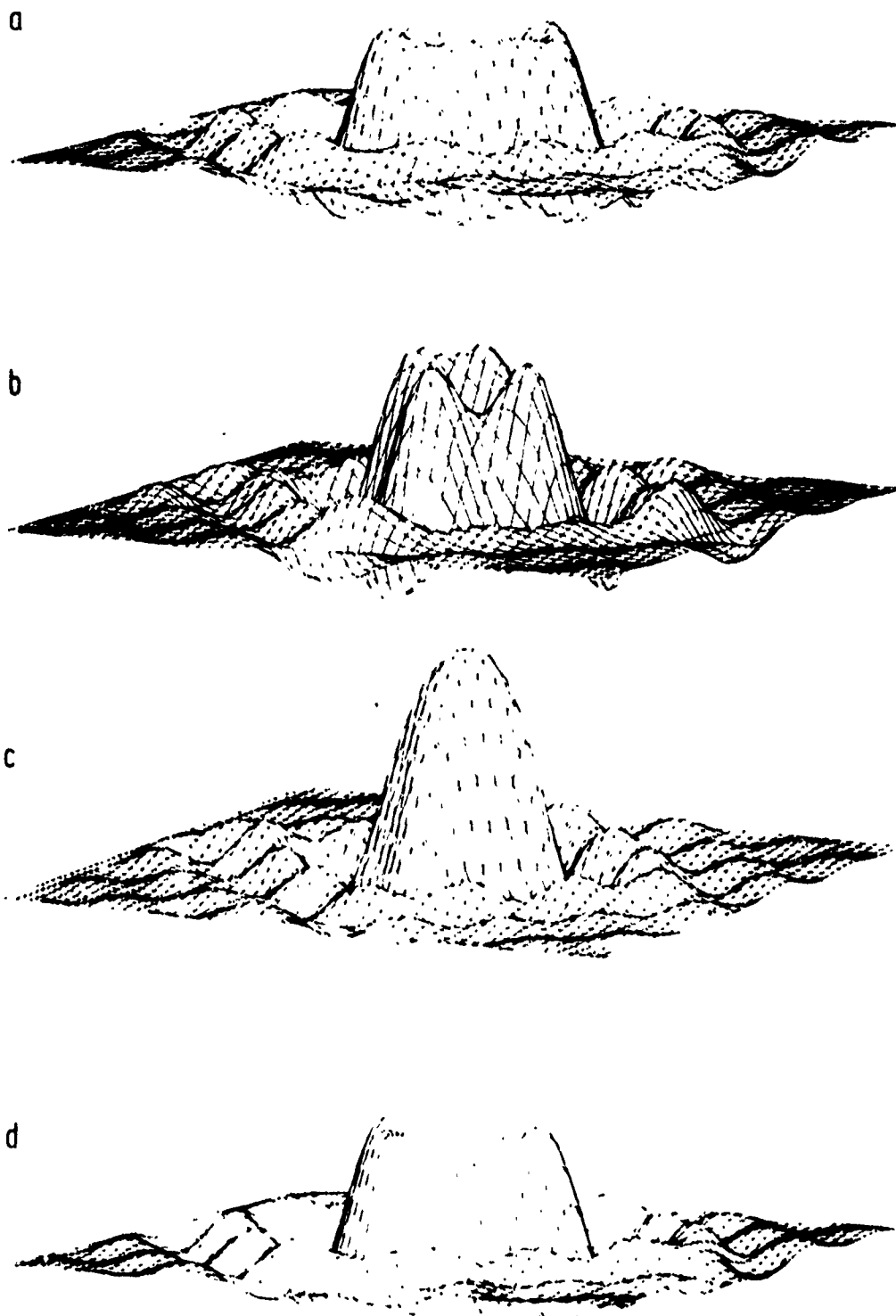
Figure 3-7.   Diffraction patterns similar to Figure 3-6 but
              for an array of 64x64 hydrophones and an
              aperture A=64d.   The focusing distance equals
              R=5A=320d.   (a) R_0=6.5A, (b) R_0=6A, (c) R_0=4.5A,
              (d) R_0=4A.   (Courtesy N. Mohamed, Government of
              Kuwait.)

Figures 3-6 and 3-7 show that the diffraction patterns are not rotationally symmetrical and that they depend slightly upon the number of hydrophones. Hence, we will consider the depth of field only for one-dimension and a large number of hydrophones.

For $R=R_0$ and a broadside look direction we obtain the familiar $\sin nX/N\sin x$ beam pattern as discussed in Appendix A. The distance between the first two zero crossings equals $2\lambda/A$. For a value of $R_0 \neq R$ we obtain a pattern with a larger angle between the zero crossings. The two values $R_0 = R_{max} > R$ and $R_0 = R_{min} < R$, for which the distance between the zero crossings is doubled to $4\lambda/A$, are of interest. The difference $R - R_{min} = R_F$ is the front depth of field, and the difference $R_{max} - R = R_B$ is the back depth of field. The sum $\Delta R_F + \Delta R_B$ is the depth of field.

The only practical way to obtain R_{max} and R_{min} is to let a computer determine the beam pattern for various values of R_0 and check for which values the distance between the first zero crossings is just twice that for $R=R_0$. The values so obtained for ΔR_F and ΔR_B, normalized by the aperture A, are plotted versus R/A for various values of λ/A in Figures 3-8 and 3-9. One may readily see that the back depth of field accounts for most of the depth of field, and that it increases much more rapidly with R/A than the front depth of field.

Focusing provides the greatest reduction in beamformer output error when the system operates just to the left of the shaded area in Figure 3-5. For a broadside signal $B=0$, the focusing circuits derived will give reasonable results anywhere to the left of the double cross-hatched area. If the particular beamformer is used in a configuration such that it operates in the lower left-hand corner of Figure 3-5, i.e. $A \leq 70$ and $A \leq 500$, Figures 3-8 and 3-9 show that the system's depth of field will be low, i.e. small errors in estimating R will result in large

60

50

40

$\Delta R_F/A \longrightarrow$

30

20

10

0

0   10   20   30   40   50   60

$R/A \longrightarrow$

A/λ

70
100

150

200

250
300
350
400
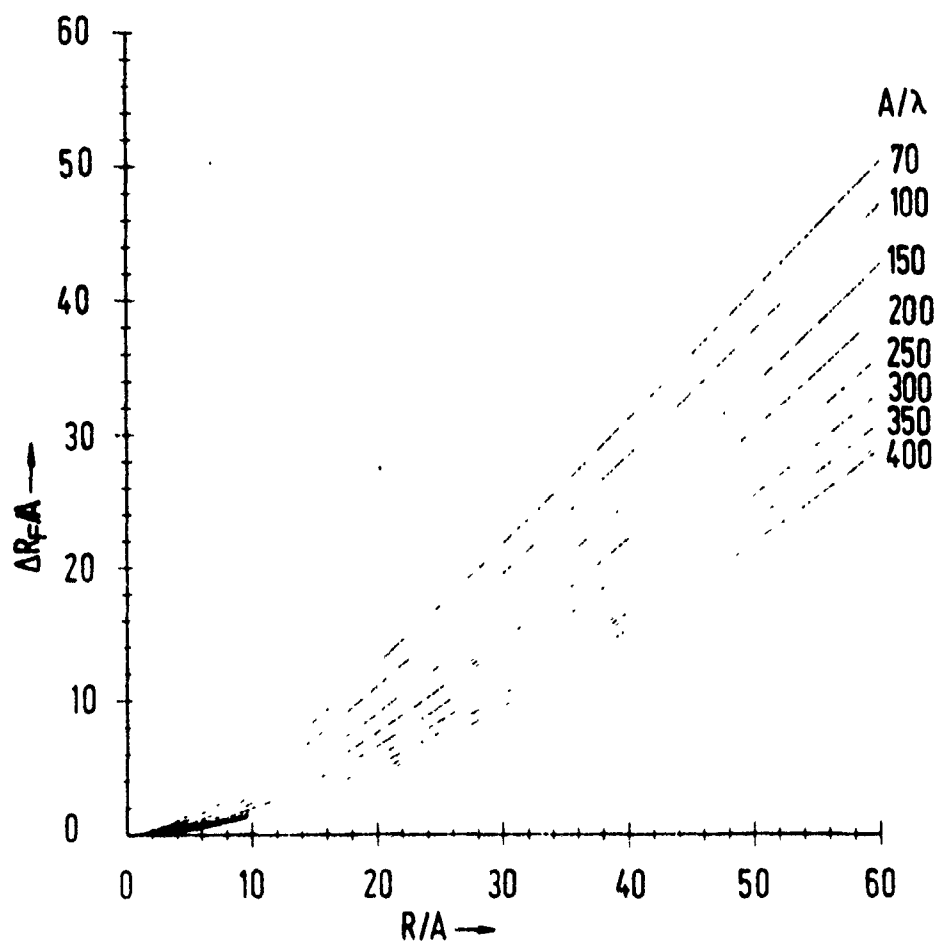
Figure 3-8.   Normalized front depth of field $\Delta R_F/A$ as a
function of the normalized focusing distance
R/A for various values of A/λ.   A = aperture,
λ = wavelength.   (Courtesy N. Mohamed,
Government of Kuwait.)
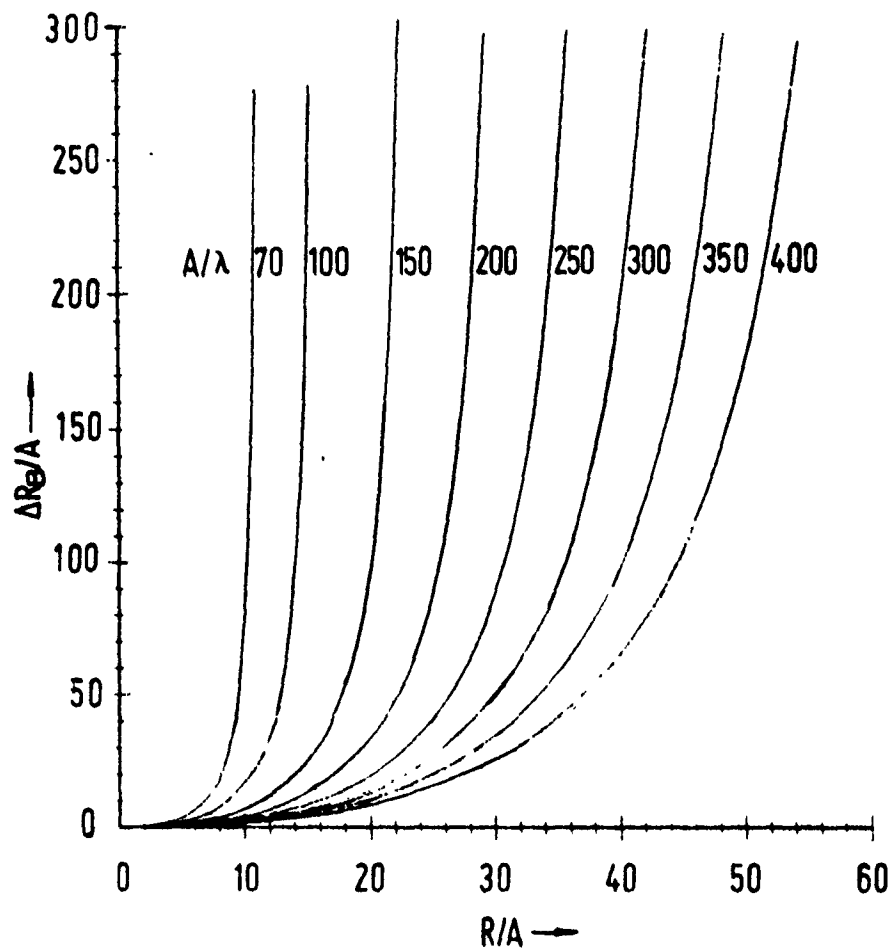
Figure 3-9. Normalized back depth of field $\Delta R_B/A$ as a
function of the normalized focusing distance
R/A for various values of A/λ.   A = aperture,
λ = wavelength.   (Courtesy N. Mohamed,
Government of Kuwait.)

3-18

beamformer output errors. In this case, an operator-
adjustable focusing capability is probably required. As
discussed in this section, this can be easily achieved with
the circuit of Figure 3-2 where the multiplication factor in
the DAC's is supplied by a microprocessor. If the
beamformer is to be operated in the unshaded upper-half of
Figure 3-5, then a reasonable approach would be to provide a
close-in fixed focusing distance and take advantage of the
resulting large backfield of view indicated in Figure 3-9.

4. HARDWARE DESCRIPTION AND TESTS

This section describes two separate hardware systems that were designed and built using the analog FFT technology. The first system built was a two-dimensional underwater acoustic imaging system that has produced motion pictures of moving targets. It is discussed in Section 4.1. The second system was a one-dimensional beamformer with a focusing capability that was tested in the laboratory. It is discussed in Section 4.2.

4.1 THE TWO-DIMENSIONAL ACOUSTIC IMAGING SYSTEM

4.1.1 Introduction

The acoustic imaging system was designed and built at The Catholic University of America in Washington, D.C. in 1973. The system consists of a square array of 16x16=256 hydrophones built by Bendix Corporation's Electrodynamics Division, and a 256 channel analog FFT receiver built at Catholic University.

The system was tested by the Applied Research Laboratories (ARL) of the University of Texas at Austin at their Lake Travis Test Station during 1974, 1975 and 1976.

Section 4.1.2 discusses the hardware in more detail and Section 4.1.3 discusses the test results.

4.1.2 Acoustic Imaging System Description

A rear view of the in-water portion of the acoustic imaging system is shown in Figure 4-1. It consists of a 100 kHz active source mounted on top of a passive receiving array. The receiving array consists of 256 hydrophones - 16 columns of 16 hydrophones each and their preamplifiers. Two preamplifiers are mounted in each protective housing, resulting in the configuration shown in Figure 4-1. The array is about 140 cm on a side, giving about 37 wavelengths
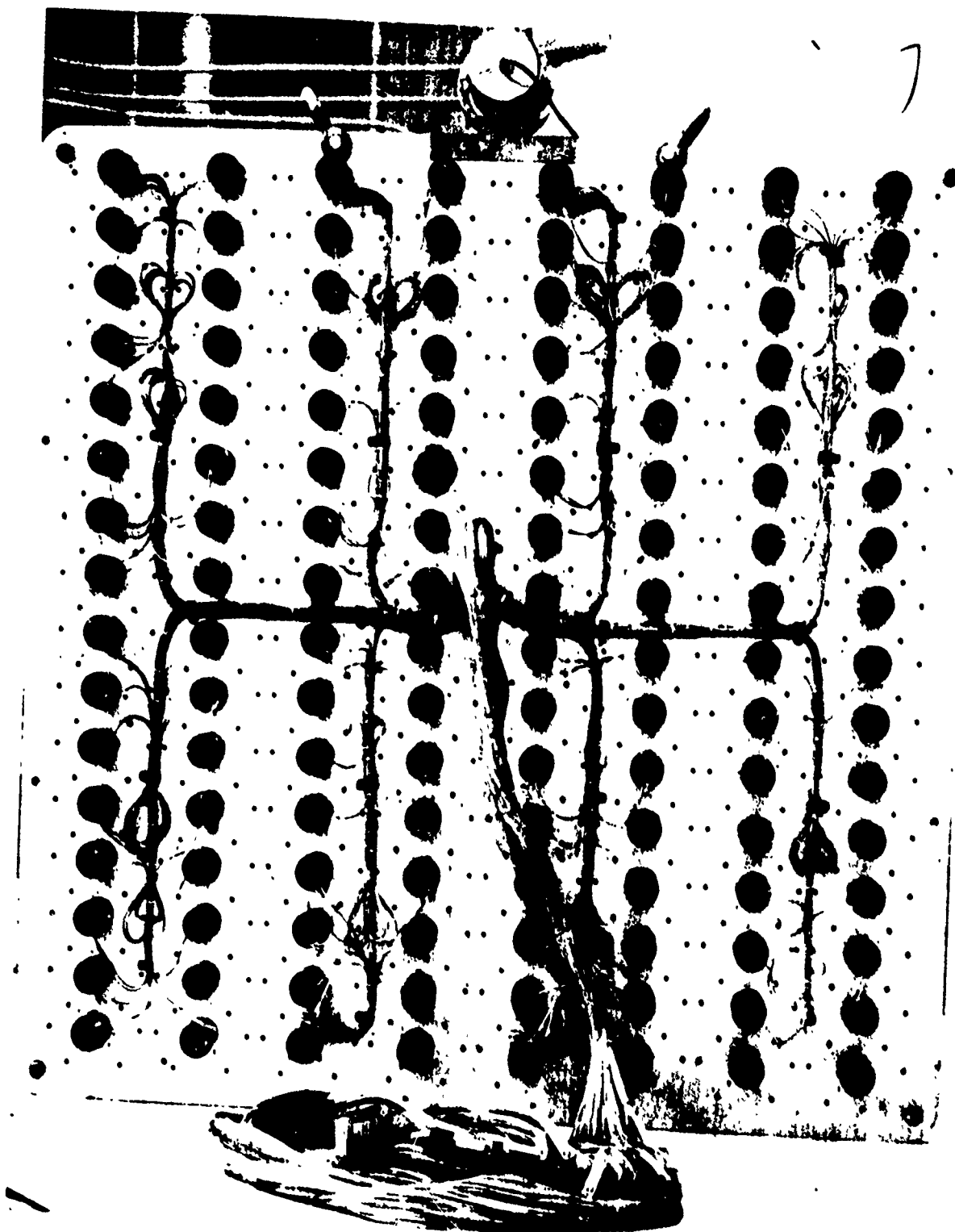
Figure 4-1. Rear side of array with 16x16 hydrophones during construction. A projector is mounted on top.

between hydrophone centers at 100 kHz. Grating lobes are about 10° off broadside in both the horizontal and vertical directions with this array design.

A conceptual view of the 256 channel processor is shown in Figure 4-2. As discussed in Section 2, the array inputs are processed by row, forming sixteen 1x16 analog FFT coefficients in the proper order. Columns of sixteen similar FFT coefficients are again FFT'ed to produce ordered two-dimensional FFT coefficients (or beams) of the input data. Since the system is analog, the coefficients are analog functions of time. The coefficients are processed for amgiguity resolution, as discussed in Section 2 and Appendix B and then displayed. The original display, shown in Figures 4-2 and 4-3, was an array of light-emitting diodes, one for each beam produced. This display was later discarded and the light-emitting diodes were not sufficiently uni orm to display half-tones. The use of a television monitor as a display solved these problems. The complete system described by Figure 4-2 occupied one standard rack, as shown in Figure 4-3.

Each of the thirty-two 1x16 analog FFT cards used in the system is similar to the circuit shown in Figure 2-4.

4.1.3 System Tests

All of the tests which are discussed here were made by the Applied Research Laboratories at their Lake Travis Test Station. The array was mounted underwater and data was taken using controlled active and passive targets.

During 1975, receiving beam patterns, dynamic range, and spatial resolution measurements in the far, intermediate and near acoustic fields were made on the system.

To measure the beam pattern, an active sound source operating at a frequency of 100 kHz was located about 500 feet from the hydrophone array. The array was then rotated and tilted to change azimuth and elevation. The
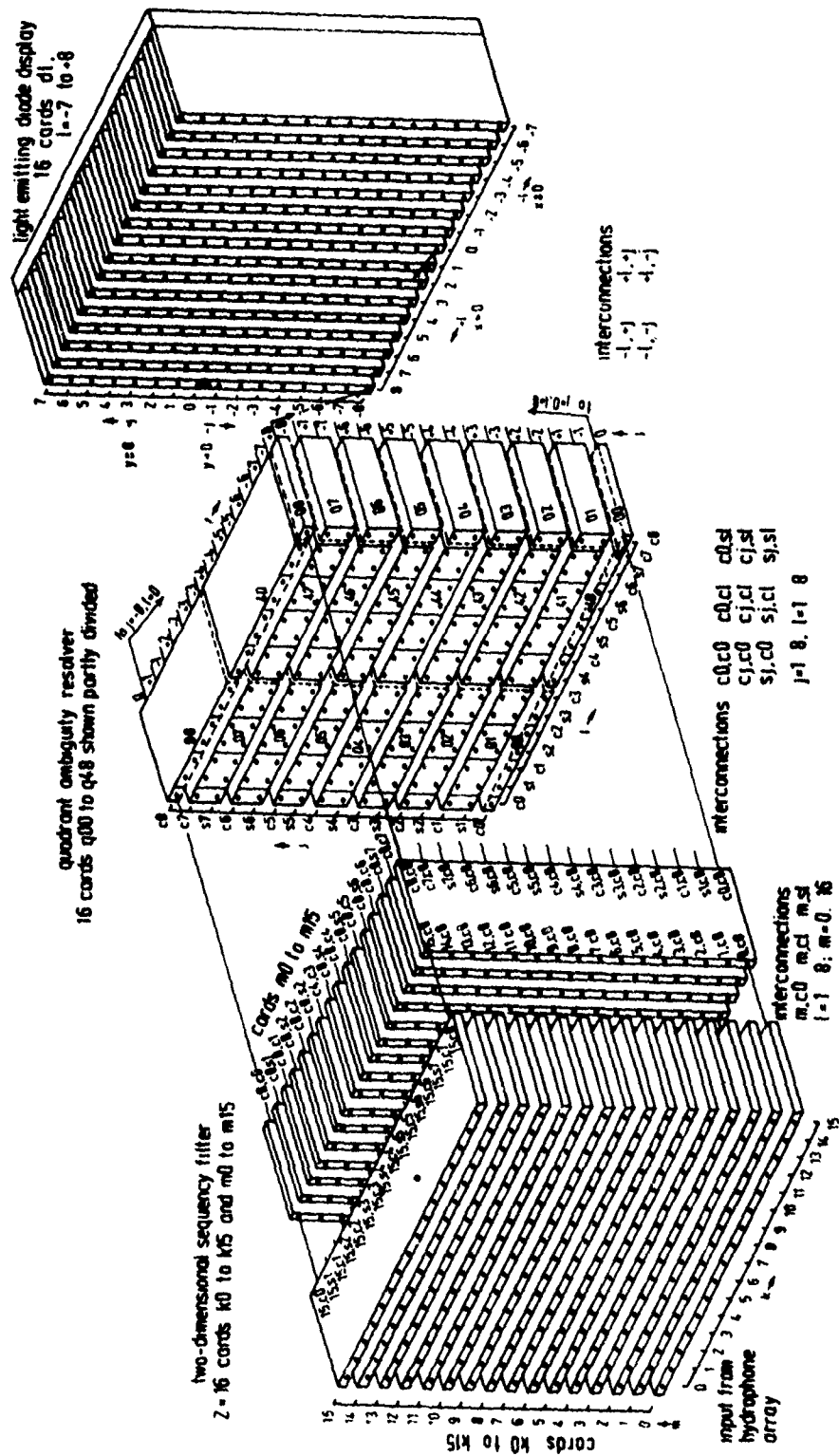
Figure 4-2. Axonometric drawing of an acoustic imaging equipment using 16x16=256 beams.
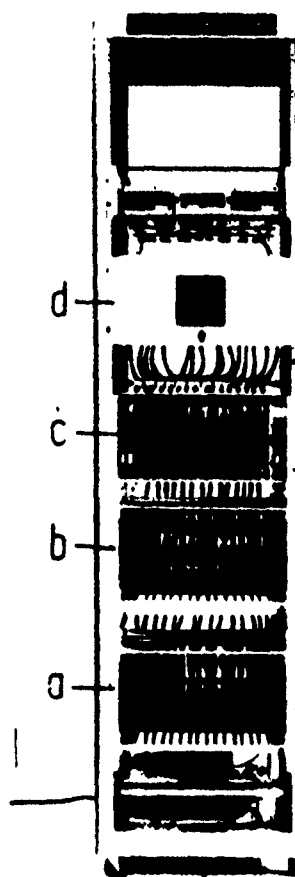
Figure 4-3. Complete processor containing a beamformer for 256 beams (a, b, c) and a light-emitting diode display (d).

light point on the light-emitting diode array display
representing the image of the sound source wandered
horizontally and vertically across the display according to
the direction of the array axis relative to the straight line
between array and sound source. Figure 4-4 shows a typical
farfield horizontal beam pattern of a single element of the
array measured at the input of its preamplifier. A typical
such farfield horizontal beam pattern measured at the input
to the display matrix is shown in Figure 4-5. The
improvement due to the beamformer is obvious. The large
amplitude lobes located at 10° intervals either side of 0°
in Figure 4-5 are the result of the element spacing in the
array. The half-power beamwidth of a lobe is nominally
0.67°. Analogous patterns measured in the intermediate and
nearfields of the array are shown in Figures 4-6 and 4-7
respectively. The latter beam appears to be collimated.
The sidelobe energy in Figure 4-6 is actually 30% of the
mainlobe energy. This compares to a theoretically-expected
value of 22%, the difference is due to the tolerances of the
hydrophone array and the processor.

Resolution of two point sources in the far field of
the array is shown in Figure 4-8. The sources were of
unequal strength. Each pattern of the drawing shows signal
level versus azimuthal angle recorded as the array was
scanned past the two sources. The angular separation of the
sources was 1.31° for the upper pattern, 1.0° for the lower
pattern. The latter separation is clearly resolved.

As mentioned in Section 4.1.2, during 1976 the Applied
Research Laboratories constructed and installed a 256 channel
multiplexer between the receiving array and the beamformer.
In addition, a television monitor was installed to replace the
light-emitting diode display. Using this improved system, a
two-dimensional distributed array of scatterers, shown in
Figure 4-9, was fabricated and installed on an underwater
rotator at the Lake Travis Test Station in the far field of
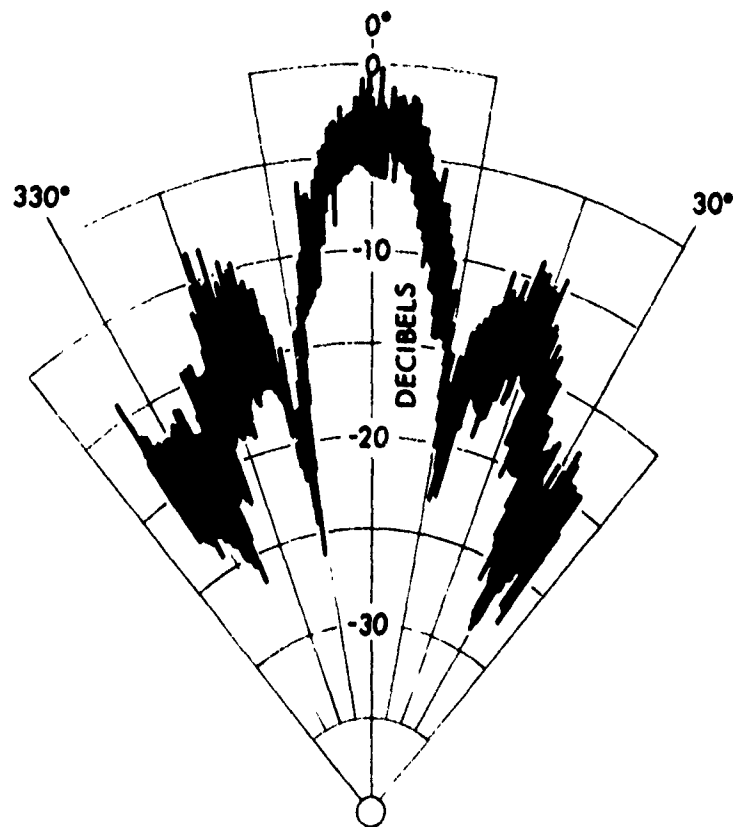
Figure 4-4. Single element farfield beam pattern.
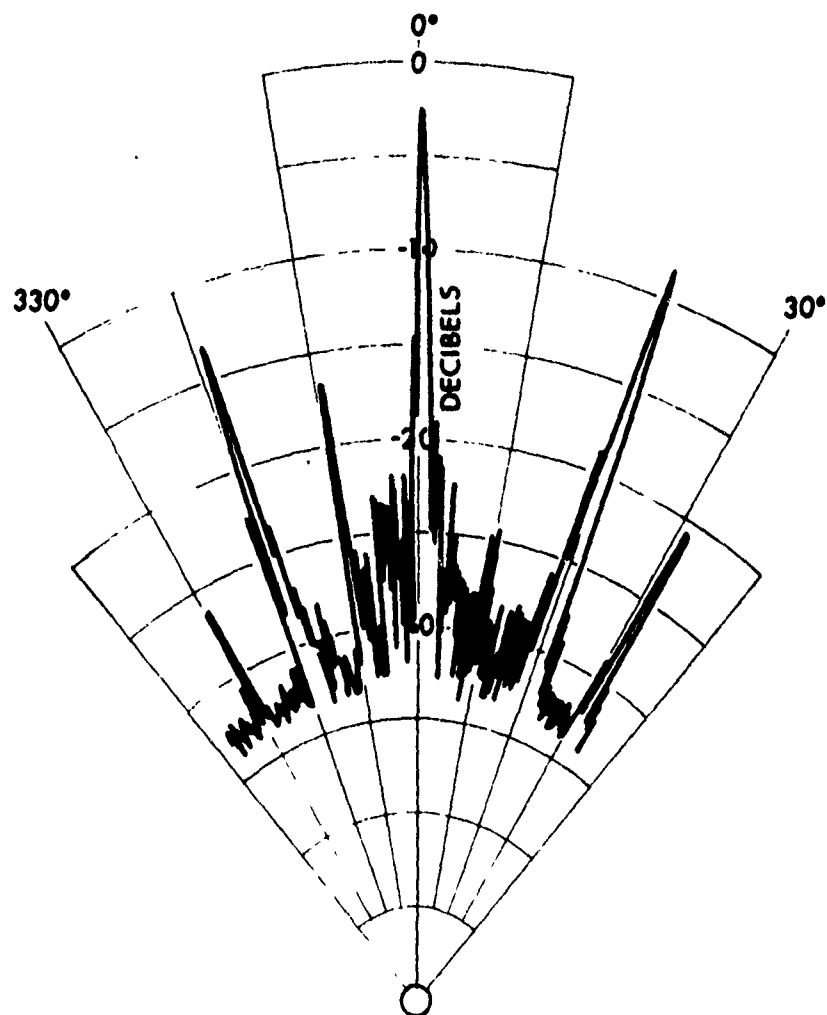
Figure 4-5. 16-element processed beam pattern, farfield.
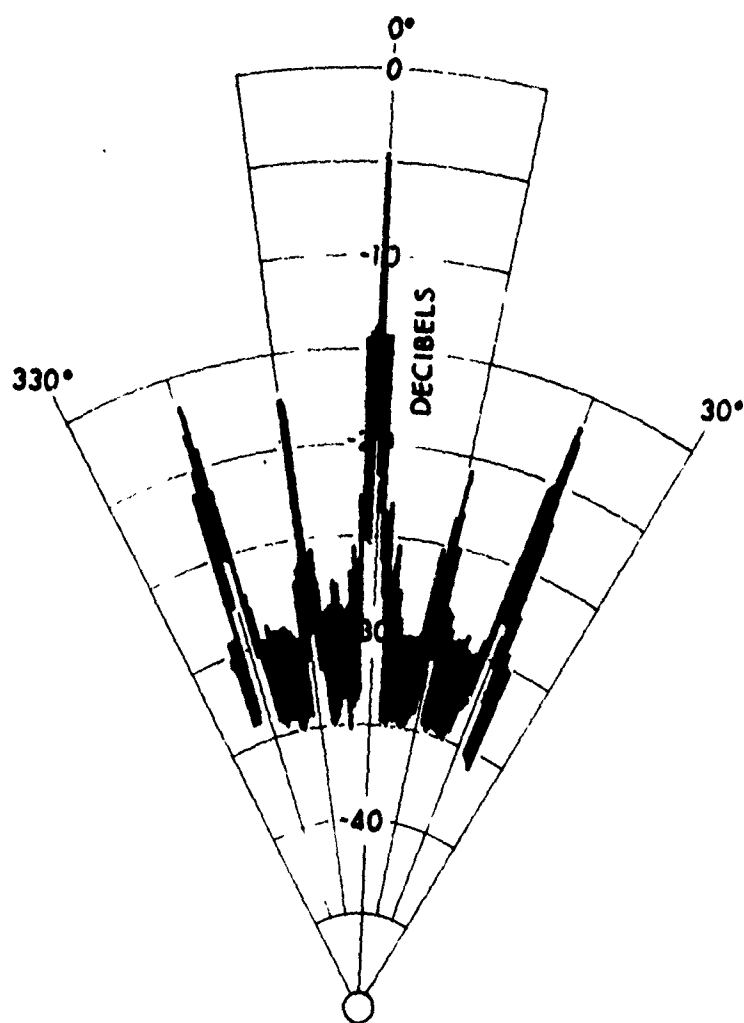
Figure 4-6. 16-element processed beam pattern, intermediate field.
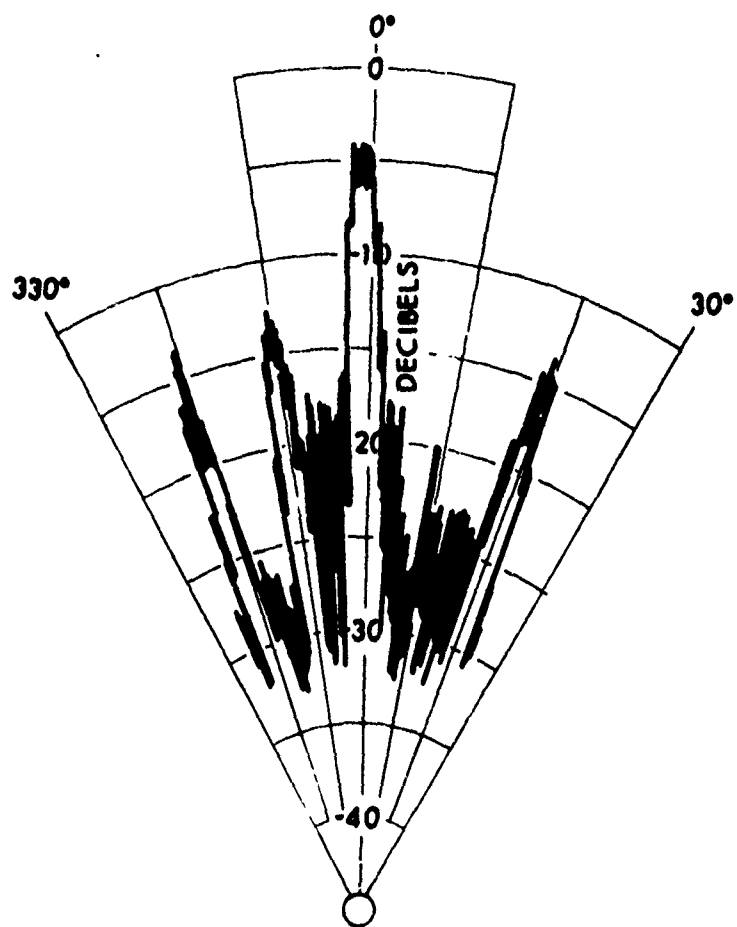
Figure 4-7.   16-element processed beam pattern, nearfield.
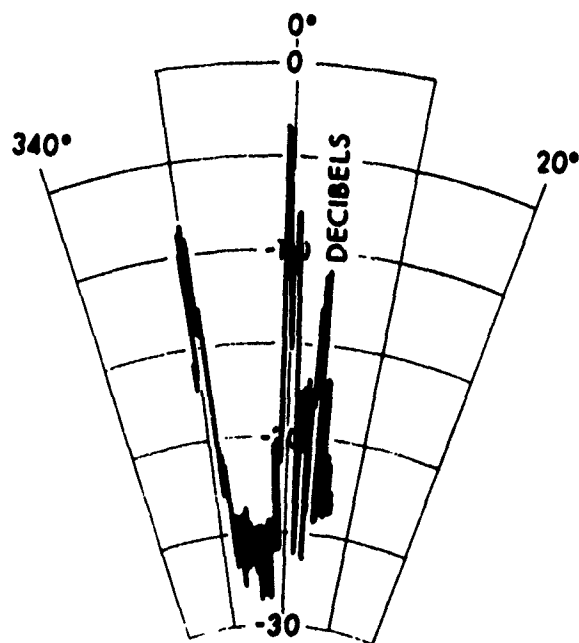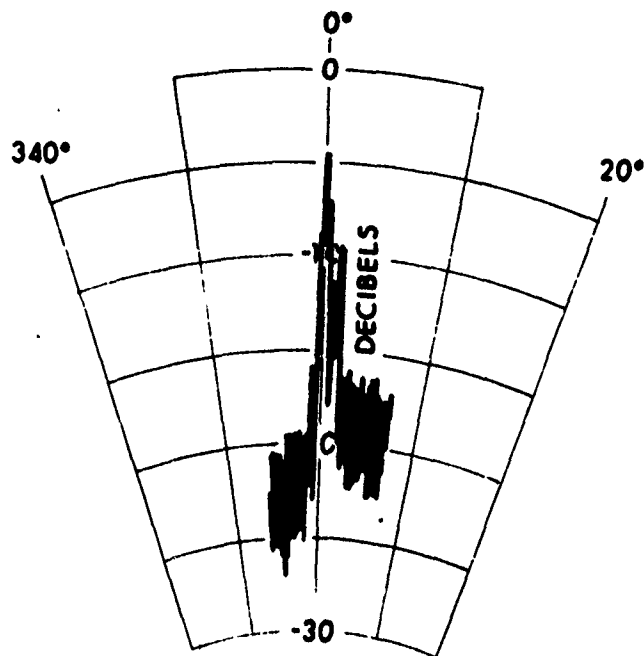
Figure 4-8. Signal amplitude versus azimuthal bearing
patterns, two-point source.
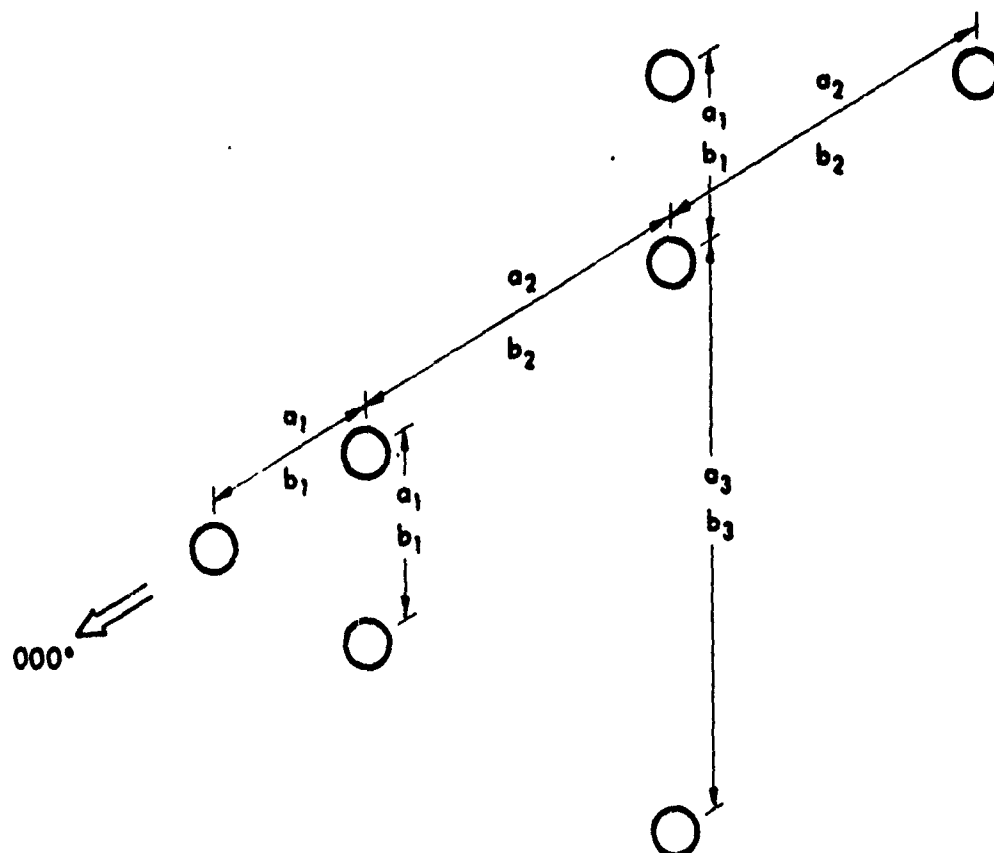
a: DISTANCE, m	b: RESOLUTION CELL SEPARATION
a_1: 1.52	b_1: 1.0
a_2: 3.35	b_2: 2.2
a_3: 4.57	b_3: 3.0

Figure 4-9.   Two-dimensional distributed target.

the array, and a 16 mm movie film of the television display as the target was totated from beam to beam was made. Selected frames from this film showing the target (a model thereof) at different aspects and the associated CRT images are shown in Figures 4-10, 4-11 and 4-12. (The brightened cells at the top right of the CRT display are caused by oscillating preamplifiers.)

The display in the movie is much easier to interpret because of information introduced by being able to see the motion of the target. However, the system does produce underwater moving images using acoustic energy. The major quality difference between normal television pictures and the pictures shown in Figures 4-10, 4-11 and 4-12 is the spatial resolution of the image. The spatial resolution of the acoustic imaging system can be increased to any desired level by increasing the number of channels in the system beyond 16x16. The next section (4.2) discusses the laboratory tests of a 64 channel beamformer. If 128 of these 64 channel beamformer systems were configured in an acoustic imaging system as shown in Figure 4-2, the resulting system would have 16 times the resolution of Figures 4-10, 4-11 and 4-12.

4.2   THE 64 CHANNEL BEAMFORMER SYSTEM

4.2.1   Introduction

The 64 channel analog beamforming system consisted of a 100 kHz analog focusing subsystem, as described in Section 3, and a 100 kHz analog FFT beamformer, as discussed in Section 2 and Appendices A and B. The actual printed circuit cards for both focusing and beamforming were designed and built at The Catholic University of America. The printed circuit cards were then fabricated into a system and tested at Undersea Research Corporation.

4-13
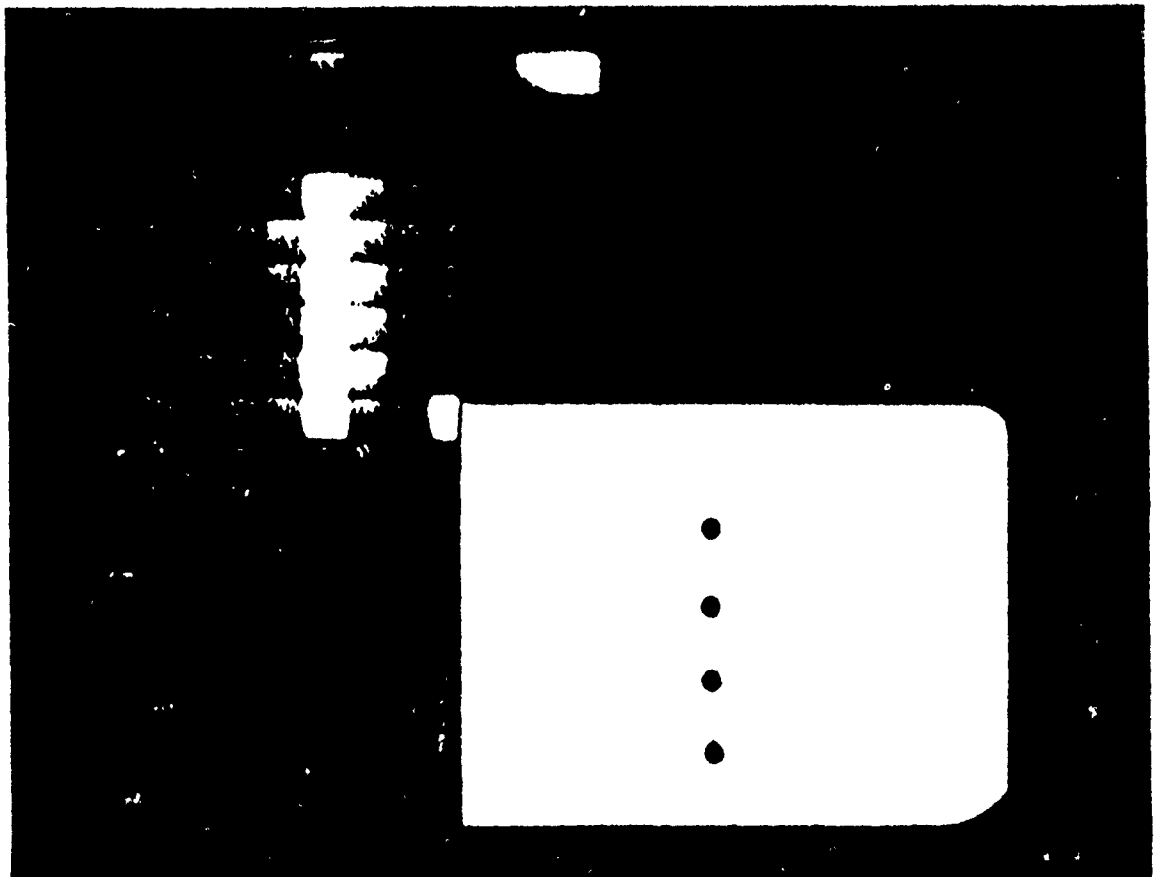
Figure 4-10. Display of a distributed target and image formed by a 16x16-element array. Φ=000°
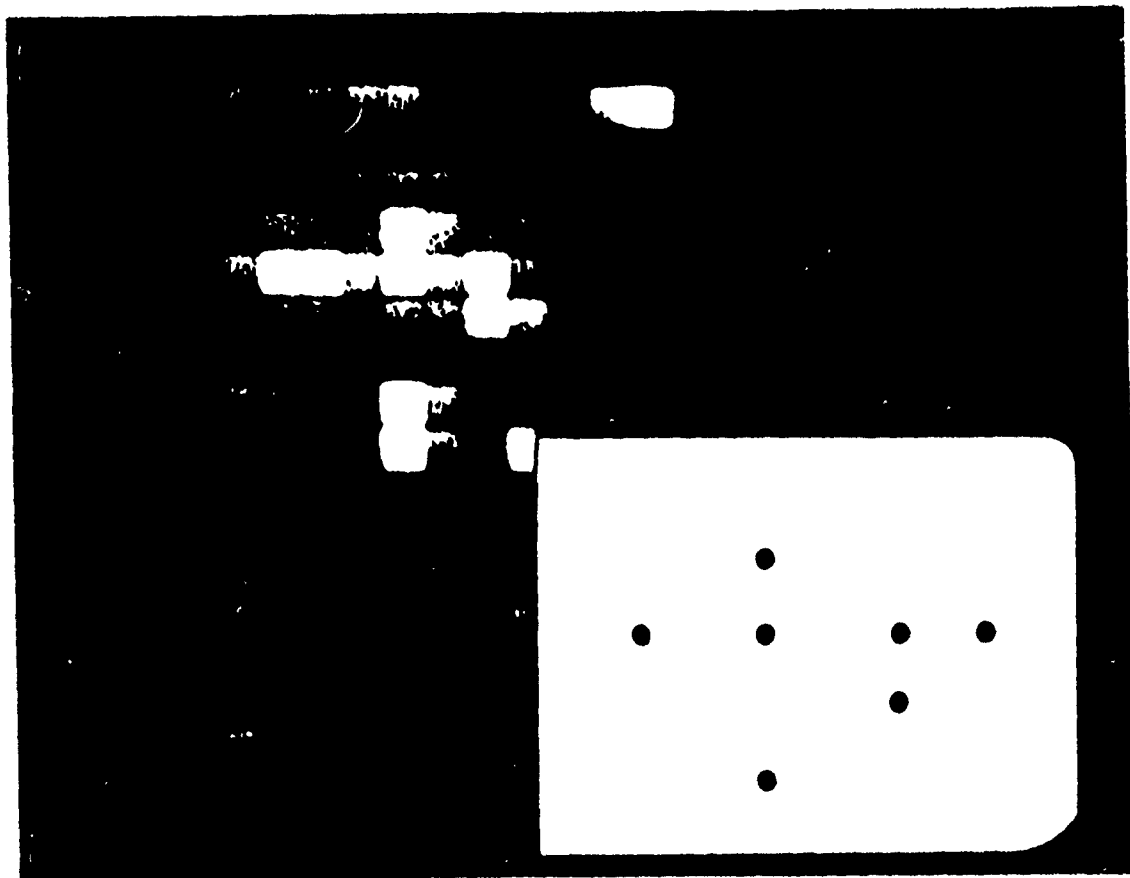
Figure 4-11. Display of a distributed target and image
formed by a 16x16-element array. $\phi=090^{\circ}$
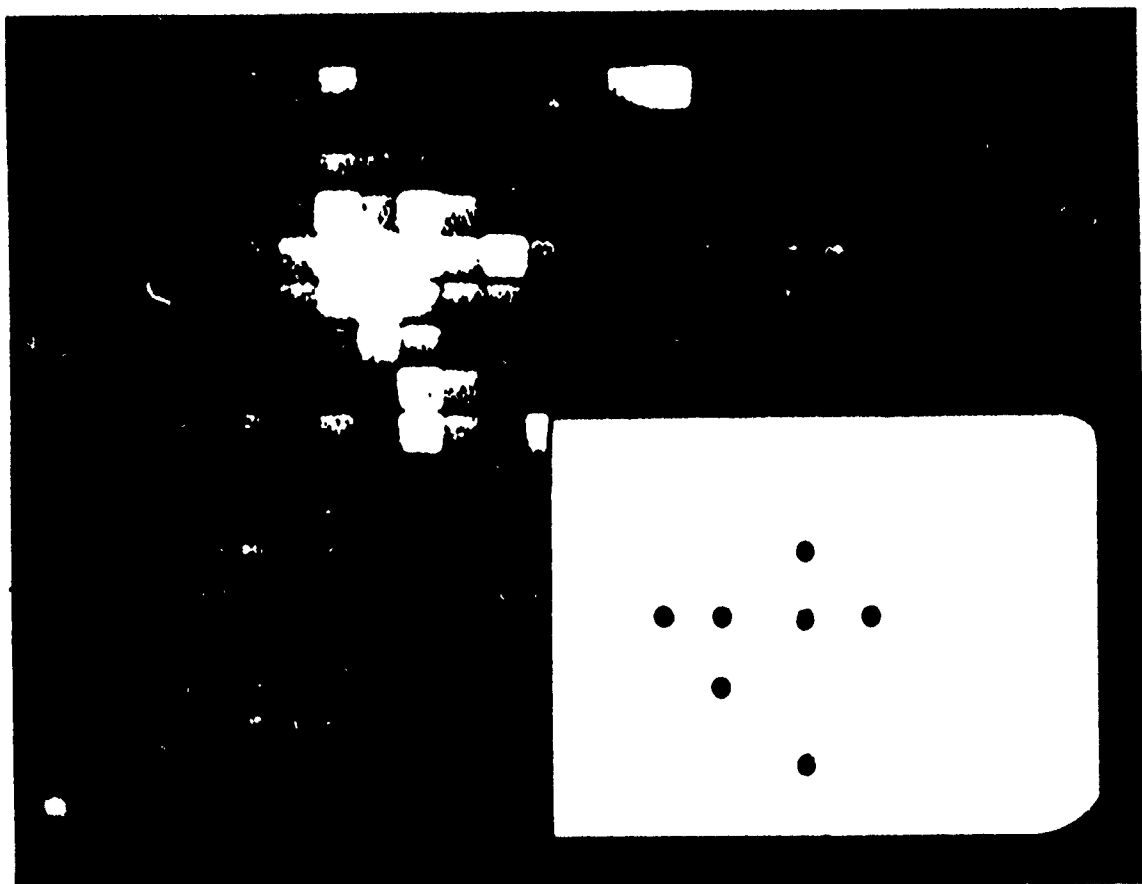
Figure 4-12. Display of a distributed target and image formed by a 16x16-element array. $\phi=330^{\circ}$

All tests were conducted in the laboratory using 100 kHz broadside input signals. This made it impossible to measure some system parameters; however, the objective of the laboratory test was to demonstrate that beamforming technology developed during this program was applicable to systems with other than 16 inputs. In addition, a more sophisticated waveform simulator was not available.

Section 4.2.2 describes the 64 channel beamformer with focusing. Section 4.2.3 discusses the testing of this system.

4.2.2 The 64 Channel Beamformer Description

The analog 64 channel beamformer consisted of four 7"x14" printed circuit cards, two analog FFT cards, and two beam ambiguity resolution cards. Each FFT card has 32 inputs and 32 outputs, and was derived using the techniques discussed in Section 2.2. The derivation of a 64 channel analog FFT is discussed in detail in Appendix A and the resulting circuit diagram is shown in Figure A-5. Each printed circuit card had 32 analog inputs, one card processed all of the odd-numbered hydrophones and calculated all of the odd-numbered sine and cosine Fourier coefficients. The other card processed all of the even-numbered hydrophones and calculated all of the even-numbered sine and cosine Fourier coefficients. This is similar to the approach taken with some digital FFT algorithms.

The beams formed to the left of broadside are the complex conjugates of the beams formed to the right of broadside. Therefore there are only 64 real coefficients out of each FFT card. To obtain independent beams, a sine coefficient (s_i) and a cosine coefficient (c_i) are processed by a beam ambiguity resolution circuit shown in Figure 2-5, each circuit puts out two independent beams $X(i)$ and $X(63-i)$. As discussed in Section 2.2, and shown in Figure A-5, the 64 channel beamformer outputs a broadside beam and 62 other beams that have their ambiguity resolved

so that they look either to the right of broadside or to the left of broadside. In addition, there is an endfire beam (represented by C32 in Table A-5) that cannot distinguish between the left and right side of the array. A printed circuit card with 16 beam ambiguity circuits processes the 64 Fourier coefficients from each FFT card.

The four printed circuit cards comprising the beam-former, two analog FFT cards, and two beam ambiguity resolution cards, were rack mounted and wired together through a back plane. Four printed circuits cards of 16 channels each for focusing the input data prior to beamforming were mounted in the same rack.

Each 7"x18" focusing card consisted of eight circuits as shown in Figure 3-5. As discussed in Section 3.2, the circuit in Section 3.5 processes data from hydrophones that are equidistant from the center of the array (i.e. hydrophones i and N-i). Because of this particular design, the focusing cards were capable of only focusing for point sources at broadside. Using the focusing circuit in Figure 3-5, 64 channels of focusing require sixty-four 8 bit words be shifted into the 64 shift registers (SN74174's in Figure 3-5). These 8 bit words determine the relative phase shift applied to each input data channel. A Texas Instruments SR-52 hand calculator and its printer were interfaced to the focusing cards as a controller. The SR-52 is programmable and programs can be stored on and read from small magnetic cards. The SR-52 was programmed to calculate the proper 8 bit binary word for each shift register and to shift these words into each register in series. Program parameters, at the operator's option, included the wavelength of the data, the hydrophone spacing, and the source distance.

The 64 channel analog beamformer system with focusing consists of four 16 channel focusing cards, an interface card for the SR-52 hand calculator and its printer, two analog FFT cards, and two beam ambiguity resolving cards.

All of the cards were mounted in a small rack and interconnected through a back plane.

4.2.3 System Tests

The allowable input signal dynamic range was measured as the difference between the system self-noise and the maximum allowable signal level. For the circuits tested it was at least 61 dB. This number is a minimum value; since the self-noise of the digital voltmeter was at least as large as the self-noise of the beamformer, the minimum detectable input signal was bounded but could not be measured.

Since only broadside input data was available, only the response of the beams in the broadside direction could be measured. Table 4-1 compares the measured and theoretically-expected response of each beam at broadside. The experimental data was taken with a 3-volt peak to peak 100 kHz broadside signal into the beamformer. The response was measured with a three and one-half place digital voltmeter. A measured response of -66 indicates that the beam response was less than the noise level of the meter. This data indicates that the system computation noise has probably moved the nulls between sidelobes off of the broadside direction. A comparison with Figures 2-6 and 2-7 shows that for beams close to broadside, deep nulls do exist in the broadside direction. It is only for beams looking in directions quite far from broadside that the null direction has been shifted off broadside. In Figure 2-6, a shift of 2° near a null can result in better than a 20 dB difference in the beam pattern's sensitivity. Therefore this data indicates that the 1x64 beamformer is producing the expected beam patterns.

The bandwidth of the beamformer is dictated by the frequency range over which the integration in the beam ambiguity circuit of Figure 2-5 results in phase shifts that are close enough to 90° to result in unique output beams.

BEAM	MEASURED RESPONSE (dB)		THEORETICAL RESPONSE (dB)
	Left of Broadside	Right of Broadside	
0	0.0		0.0
1	-59.3	-65.3	-237.9
2	-45.2	-46.2	-240.4
3	-40.2	-59.3	-242.6
4	-44.5	-44.5	-231.8
5	-49.8	-53.3	-229.7
6	-59.3	-59.3	-248.5
7	-53.3	-49.3	-236.6
8	-39.3	-44.5	-233.6
9	-48.4	-45.3	-251.8
10	-66.0	-66.0	-239.5
11	-59.3	-65.3	-236.2
12	-38.1	-38.5	-254.1
13	-51.3	-48.4	-241.5
14	-66.0	-66.0	-237.1
15	-65.3	-66.0	-255.8
16	-66.0	-55.8	-241.5
17	-66.0	-66.0	-238.4
18	-46.2	-48.4	-248.3
19	-38.4	-39.7	-242.6
20	-59.3	-65.3	-239.4
21	-59.3	-49.8	-218.8
22	-43.0	-42.4	-233.0
23	-35.5	-35.5	-227.2
24	-66.0	-66.0	-222.6
25	-66.0	-66.0	-239.8
26	-41.2	-39.7	-239.8
27	-66.0	-66.0	-227.8
28	-45.3	-47.3	-224.4
29	-34.2	-44.5	-220.9
30	-59.3	-55.8	-240.1
31	-36.7	-37.0	-230.6

Table 4-1. Beamformer broadside response to a broadside 100 kHz signal.

From the derivation in Appendix B it can be shown that if the resulting phase shift, $90° \pm 5°$, is such that $\sin\theta$ is small compared to 1, then unique beams will result. $\sin\theta < 0.1$ when $\theta < 5°$. Figure 4-13 shows the measured phase shift resulting from the integration circuit of Figure 2-5. In this case, for a design frequency of 100 kHz, $\sin\theta < 0.1$ over a bandwidth of 80 kHz.

The input signal dynamic range for the four focusing cards was measured to be approximately 45 dB. The DAC's on the focusing cards were loaded from the SR-52 for an array with a half wavelength spacing between hydrophones at 100 kHz, and a point source 10 m from the array. A 100 kHz sine wave was the input signal on all channels. Figure 4-14 compares the expected phase shift on each hydrophone relative to the two hydrophones closest to the center of the array, to the measured phase shift at the output of the focusing cards.

There is good correlation between the measured data and the expected data; the maximum error is approximately $\lambda/24$. Some of these errors are due to problems in estimating the hydrophone-to-hydrophone phase differences from an oscilloscope. However, a larger portion of the errors are due to quantization errors caused by using 8 bit DAC's. These errors could be reduced to any desired level by increasing the word length used to represent the phase multiplication term in Equation (3-14).
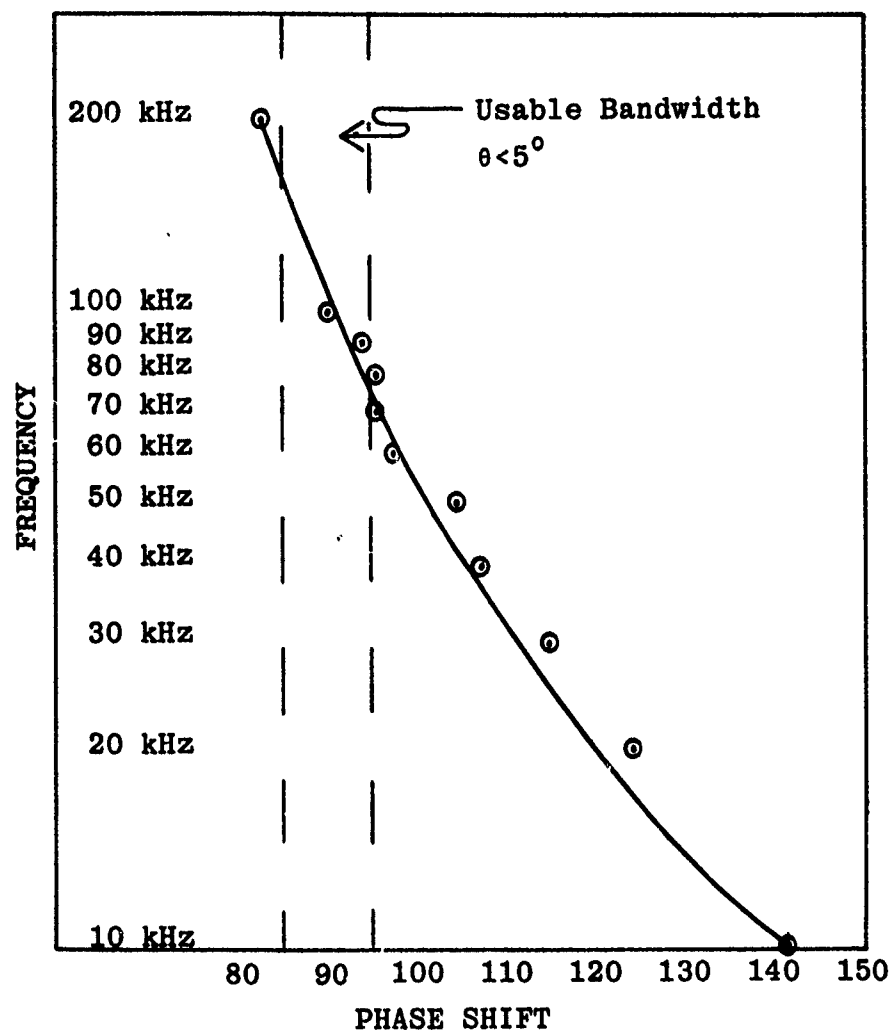
Figure 4-13. Beam ambiguity resolving circuit phase shift
as a function of input frequency. The
resulting usable system bandwidth is shown
between the dashed vertical lines.
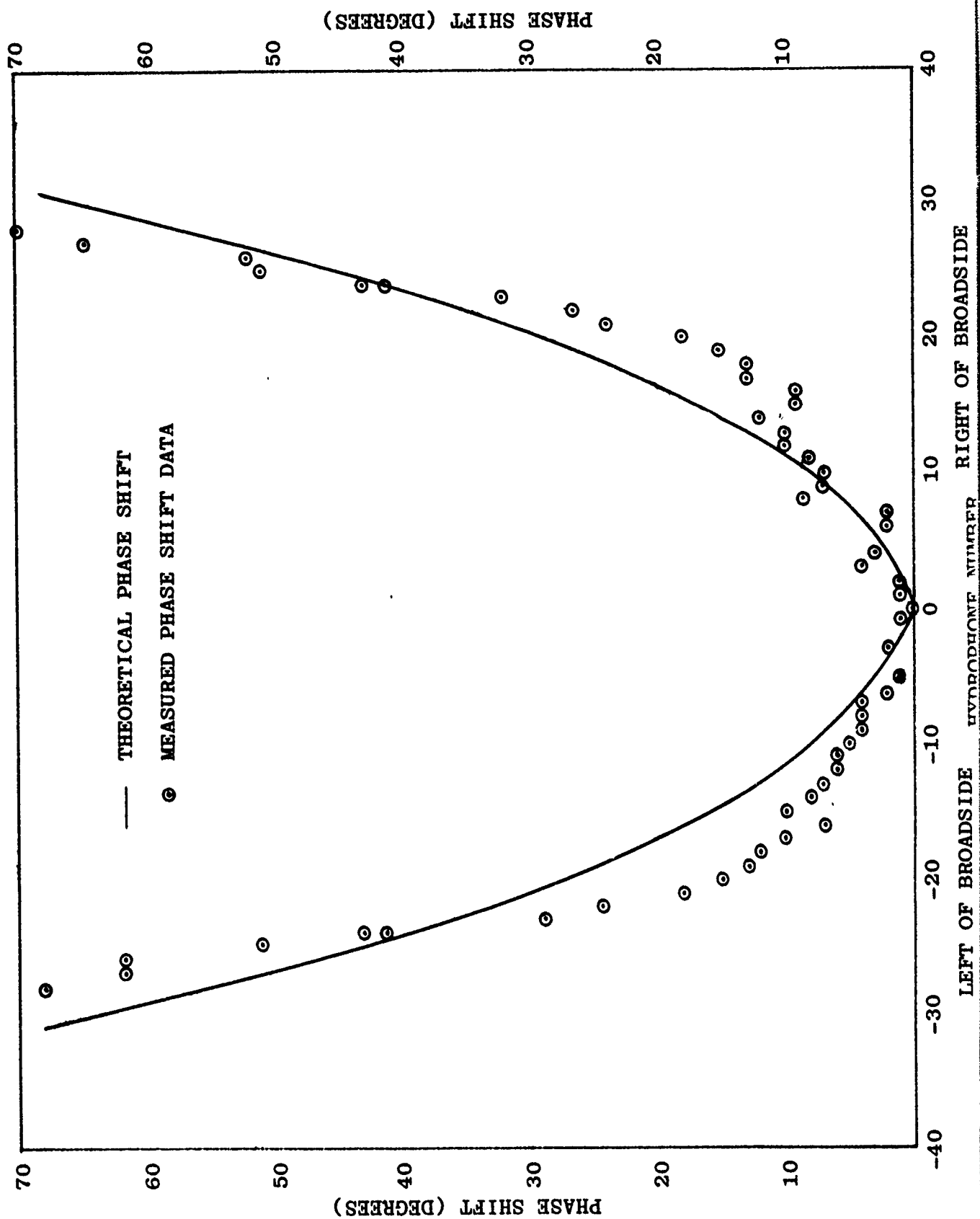
Figure 4-14. A comparison of the theoretical and expected
phase shift for d=λ/2, R=10m and a 100 kHz
signal.

5. PRODUCTION SYSTEM PACKAGING TECHNIQUES

5.1 INTRODUCTION

In this section the major types of advanced electronic production packaging techniques will be introduced, briefly described, and compared to one another with respect to the packaging needs of the analog FFT beamformer. The four types of packaging to be discussed are:

a. MSI IC's with resistor chips and capacitor chips
b. Hybrid packages
c. Semi-custom LSI
d. Custom LSI

5.2 TECHNICAL DISCUSSION

By using MSI technology, 4 operational amplifiers may be put into a 16-pin Dip package. Clusters of 10 to 12 resistors may be put into the same type package, and 6 to 8 capacitors may also be housed in this manner. For interconnectors, PC board or wire wrap socket board media may be used.

Using thick film substrate technology, hybrid circuitry would integrate the operational amplifiers, the resistors and small value capacitors in a metal can. One such metal can of 1"x1" size could house 10 operational amplifiers with 50 associated resistors and 10 small capacitors. These metal cans would fit into PC board type media for interconnection.

Semi-custom LSI consists of chips that have a set number of uncommitted transistors and resistors in one Dip-type package. For example, a 24-pin Dip could have 40 to 50 operational amplifiers with associated resistors and some small capacitors. The customer can send the schematics to the manufacturer and have the circuit laid out, or can receive a "kit" enabling him to lay out his own LSI circuit much like a PC board.

Custom LSI is laid out specifically to the customer's needs and can vary in package type, size, internal components, etc. depending upon the customer's requirements.

A comparison of these four different types of packaging systems for a 1x64 analog beamformer system first shows that they all can meet the following requirements: 1-2 MHz bandwidth, 2-3 V/µs slew rates on the operational amplifiers, noise floor 60-70 dB down, component tolerances of 0.5% absolute and 0.1% relative for resistors, and ample dynamic range. All packaging systems can be second-sourced although it is sometimes difficult to find multiple sources for custom LSI.

Table 5-1 compares power, size of packages, minimum production levels and overall cost for the four different types of systems. The data in Table 5-1 can easily be extrapolated to other size beamformers. For example, the size, power and number of chips for a 16 channel beamformer are one-fourth of that shown in this table; the cost for a 16 channel beamformer are given in the table. In this example, the cost does not quite go down by a factor of 4 in the MIS and hybrid systems. This is because of one-time fixed costs on things like checkout, PC board design and chip design on hybrid systems, even though fixed costs are amortized over 120 systems because of the minimum 1000-chip order for hybrids.

In semi-custom and custom LSI the cost does drop by a factor of four because of the increased number of systems — 5000 and 10000 — used to amortize prices, and because most of the cost is in the unit price of a chip.

5.3   CONCLUSIONS

System costs and power dissapation seem to drop drastically when semi-custom or custom LSI are used, but this means a minimum of 1000 systems. If the 2500 system level is met, custom LSI may be used and the semi-custom LSI

Custom LSI is laid out specifically to the customer's needs and can vary in package type, size, internal components, etc. depending upon the customer's requirements.

A comparison of these four different types of packaging systems for a 1x64 analog beamformer system first shows that they all can meet the following requirements: 1-2 MHz bandwidth, 2-3 V/µs slew rates on the operational amplifiers, noise floor 60-70 dB down, component tolerances of 0.5% absolute and 0.1% relative for resistors, and ample dynamic range. All packaging systems can be second-sourced although it is sometimes difficult to find multiple sources for custom LSI.

Table 5-1 compares power, size of packages, minimum production levels and overall cost for the four different types of systems. The data in Table 5-1 can easily be extrapolated to other size beamformers. For example, the size, power and number of chips for a 16 channel beamformer are one-fourth of that shown in this table; the cost for a 16 channel beamformer are given in the table. In this example, the cost does not quite go down by a factor of 4 in the MIS and hybrid systems. This is because of one-time fixed costs on things like checkout, PC board design and chip design on hybrid systems, even though fixed costs are amortized over 120 systems because of the minimum 1000-chip order for hybrids.

In semi-custom and custom LSI the cost does drop by a factor of four because of the increased number of systems — 5000 and 10000 — used to amortize prices, and because most of the cost is in the unit price of a chip.

5.3   CONCLUSIONS

System costs and power dissapation seem to drop drastically when semi-custom or custom LSI are used, but this means a minimum of 1000 systems. If the 2500 system level is met, custom LSI may be used and the semi-custom LSI

price is cut in half. At LSI level, wiring, cost of PC
board and unit chip prices comprise most of the cost. Fixed
costs are amortized out to insignificant values at these
system quantities.

At small system quantities — 1 to 30 — it seems that
hybrid and MSI chip structures are close in cost and one
seems to show little advantage over the other. Both are in
ranges of 6 to 12 times the cost of the semi-custom LSI and
custom LSI respectively.

6. TECHNOLOGY APPLICATIONS

6.1 INTRODUCTION

This section discusses potential applications for the technology described in this report. Section 6.2 discusses this technology as applied to underwater beamforming. Section 6.3 discusses underwater acoustic imaging. Section 6.4 discusses using the focusing card technology for a waveform simulator.

6.2 UNDERWATER BEAMFORMING

The analog FFT ~atial filter can be used as a hydrophone beamformer for several array configurations. As discussed above, this type of beamformer is simple, small, inexpensive, has low power dissapation, low computation noise, high data throughput rate, and is easy to maintain. It can be made for arrays of $2^m 3^n 5^p$ by $2^q 3^r 5^s$ hydrophones. The particular choice of hardware implementation and hardware component tolerances would depend upon the particular beamformer application such as a sonobuoy, a long fixed array, or a long towed array.

The design and performance details of this application are discussed in Sections 2 and 4 and in Appendices A and B of this report.

6.3 UNDERWATER ACOUSTiC IMAGING

As discussed in Section 4, a two-dimensional underwater acoustic imaging system with 225 resolution cells has been built and successfully tested using this technology. Tne major trade-off in designing such a system is its size and cost versus its spatial resolution.

Two application areas that have been identified and aggressively investigated for underwater acoustic imaging are high value target surveillance, and providing moving pictures of work operations being conducted in turbid waters.

Potentially, the performance improvement over other technologies in both of these areas is very high. However, both of these applications require relatively high spatial resolutions and therefore relatively high costs for a prototype development.

6.4 WAVEFRONT SYNTHESIZER

The testing of sonar receivers often requires the use of synthetically-generated off-broadside data. However, the cost of generating such data is usually prohibitively expensive and few such waveform simulation facilities exist. The technology used in developing the focusing subsystem, as discussed in Section 3, provides a cheap, flexible approach to developing waveform simulators that could be used to interface to the input channels of a sonar receiver or could interface to general purpose computers for testing software array processing algorithms.

As discussed in Section 3, the circuit shown in Figure 3-2 phase shifts the analog output signal relative to the input signal by multiplying the input signal by a complex filter coefficient. The filter coefficients are calculated by a digital controller (an SR-52 programmable hand calculator in this case) and fed into the shift registers. For N input channels, N such circuits are required; each shifts the input data by a different amount.

If an N channel signal with a desired source direction and structure, i.e. plane wave, etc., is required then 2N coefficients are calculated and shifted into the corresponding shift register by the controller. A single channel of broadside signal is fed into all of the input channels simultaneously and N channels of the desired analog signal waveform are available at the system output. If an N channel system is built, it can be used for applications when only n channels, $n \leq N$, are required, where the number of channels used, n, is a software operating parameters controlled by the operator.

Such a system would be small, inexpensive, and of
potentially great utility to Navy sonar processing test
programs.

7. CONCLUSIONS

The feasibility of using two-dimensional hard-wired analog FFT beamformers as spatial filters to produce television-like images using sound waves in water has been demonstrated:

- Beamformers employing this technology can be tailored to fit most array sizes, either one- or two-dimensional.
- The circuitry is inexpensive, reliable, compact, and requires very low power.
- Very high throughput rates per channel are achievable.

Focusing circuits employing this technology have been designed, built, and laboratory tested:

- The potential use of the focusing circuit design as a wavefront synthesizer is practical.
- A system, if built, would be small in size, inexpensive, and of great utility to U.S. Navy sonar processing developient and test programs.

REFERENCES

1. Brown, D. H.   The Effects of Error in High Resolution Sonar Arrays.

2. Harmuth, H. F.   Acoustic Imaging with Electronic Circuits.   To be published by the Academic Press, New York, in 1978.

3. Harmuth, H. F.   "Generation of Images by Means of Two-Dimensional Spatial Electric Filters," Advances in Electronics and Electron Physics, No. 41, 1976, pp. 167-248.

4. Harmuth, H. F.   Sequency Theory — Foundations and Applications, Academic Press, New York, 1977.

5. Mohamed, N.   "Generation of Images by Means of Sound Waves Using a Two-Dimensional Hydrophone Array and a Sampling Filter Processor," Ph.D. Thesis, School of Engineering, The Catholic University of America, Washington, D.C.

6. Oppenheim, A. V., and Weinstein, C. J.   "Effects of Finite Register Length in Digital Filtering and the Fast Fourier Transform," IEEE Proceedings, Vol. 60, No. 8, August 1972.

7. Tufts, D. W., Hershey, H. S., and Mosier, W. E. "Effects of FFT Filter Coefficient Quantization on Bin Frequency Response," IEEE Proceedings, January 1972.

8. Weinstein, C. J.   "Quantization Effects in Digital Filters," MIT Lincoln Laboratories Technical Report 468, ASTIA Document DDC AD-706862, November 21, 1969.

APPENDIX A

ANALOG FFT CIRCUIT DERIVATION

FOR

32 CHANNEL AND 64 CHANNEL BEAMFORMERS

This appendix demonstrates the derivation of the one-dimensional analog FFT circuits for 32 and 64 inputs in Section 2.1 for 16 inputs.

The reader should notice that the algorithm derivation demonstrated here is actually just a radix 4 decimation in frequency approach. However, the real and imaginary portion of the complex filter coefficients are considered separately and this results in a net savings in the number of analog multiples required.

The discrete Fourier transform is given by

$$X(k) = \sum_{n=0}^{N-1} x(n) \varepsilon^{-j\frac{2\pi}{N}kn} \qquad k=0,1,2,\ldots,N-1 \quad (A-1)$$

$$= \sum_{n=0}^{N-1} x(n) \left[\cos \frac{2\pi}{N}kn - j \sin \frac{2\pi}{N}kn \right] \qquad (A-2)$$

$$k=0,1,2,\ldots,N-1$$

where $X(k)$ is the output beam, k; N is the number of input channels or hydrophones; and $x(n)$ is the time trace of data received by the nth hydrophone.

It can be shown that if the input data $x(n)$ is real, only $\frac{N}{2}$ independent output beams will be formed. That is $X(i)$ will equal the complex conjugate of $X(N-1-i)$. This follows from the following properties of $\varepsilon^{-j\frac{2}{N}kn}$:

$$\epsilon^{j\frac{2\pi}{N}kn} = \epsilon^{-j\frac{2\pi}{N}(N-n)} \qquad (A-3)$$

$$\epsilon^{-j\frac{2\pi}{N}kn} = \epsilon^{-j\frac{2\pi}{N}k(N+n)} = \epsilon^{-j\frac{2\pi}{N}(k+N)n} \qquad (A-4)$$

While this appendix will only demonstrate the approach for N=32 and N=64, it should become obvious to the reader that the technique will work any $N = 2^k 3^m 5^n$ where k,m,n = 0,1,2,..., and that the analog implementation shown here will give reasonable results as long as the number of inputs to each operational amplifier is kept small.

N=32 Channels

For N=32, Equation (A-2) becomes

$$X(k) = \sum_{n=0}^{31} x(n) \left[\cos \frac{\pi}{16}kn - j \sin \frac{\pi}{16}kn \right] \qquad (A-5)$$

For k=1, $\cos \frac{\pi}{16}n$ equals 1 for n=0; equals w for n=1; equals v for n=2; etc., where w,v, etc. are the values shown in Figure A-1. For k=i, $\cos \frac{\pi}{16}kn$ equals 1 for n=0; for n=1, $\cos \frac{\pi}{16}k = \cos \frac{\pi}{16}i$ equals the value i terms counterclockwise from 1 in Figure A-1. That is, if i=2 then $\cos \frac{\pi}{16}i = v$; if i=3 then $\cos \frac{\pi}{16}i = u$; and so on. For n=2, $\cos \frac{\pi}{16}i2$ equals the value 2i terms counterclockwise from 1, and so on for all n≤N-1.

The values of $\sin \frac{\pi}{16}kn$ follow from Figure A-1 in the same manner that the cosine values did except that they begin at zero for k,n=0 and go counterclockwise depending on the values of k and n.

Let the 32 input channels x(n), n = 0,1,...,31 be presented by capital letters as shown at the top of Figure A-2, where x(0)=A, x(1)=B, x(2)=C, and so on. The
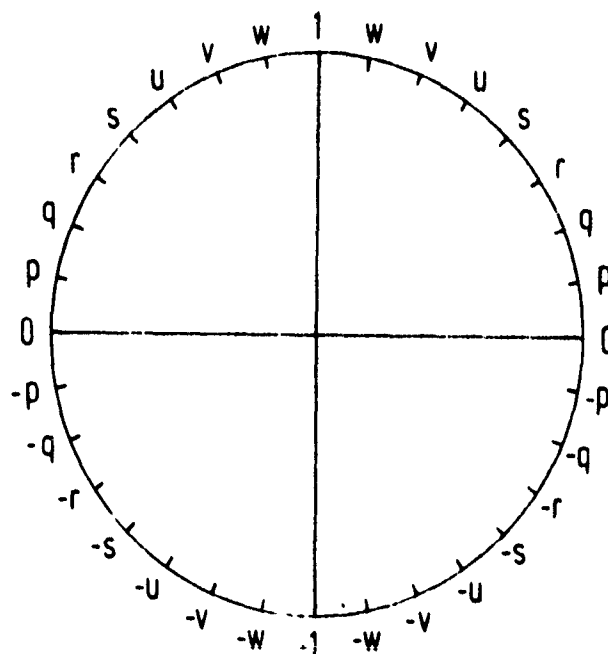
Figure A-1. Determination of the samples 0, ±p, ±q, ..., ±1 of the first 32 functions of the Fourier series. p=sin π/16, q=sin π/8, r=sin 3π/16, s=sin π/4=√2/2, u=sin 5π/16, v=sin 3π/8, w=sin 7π/16.
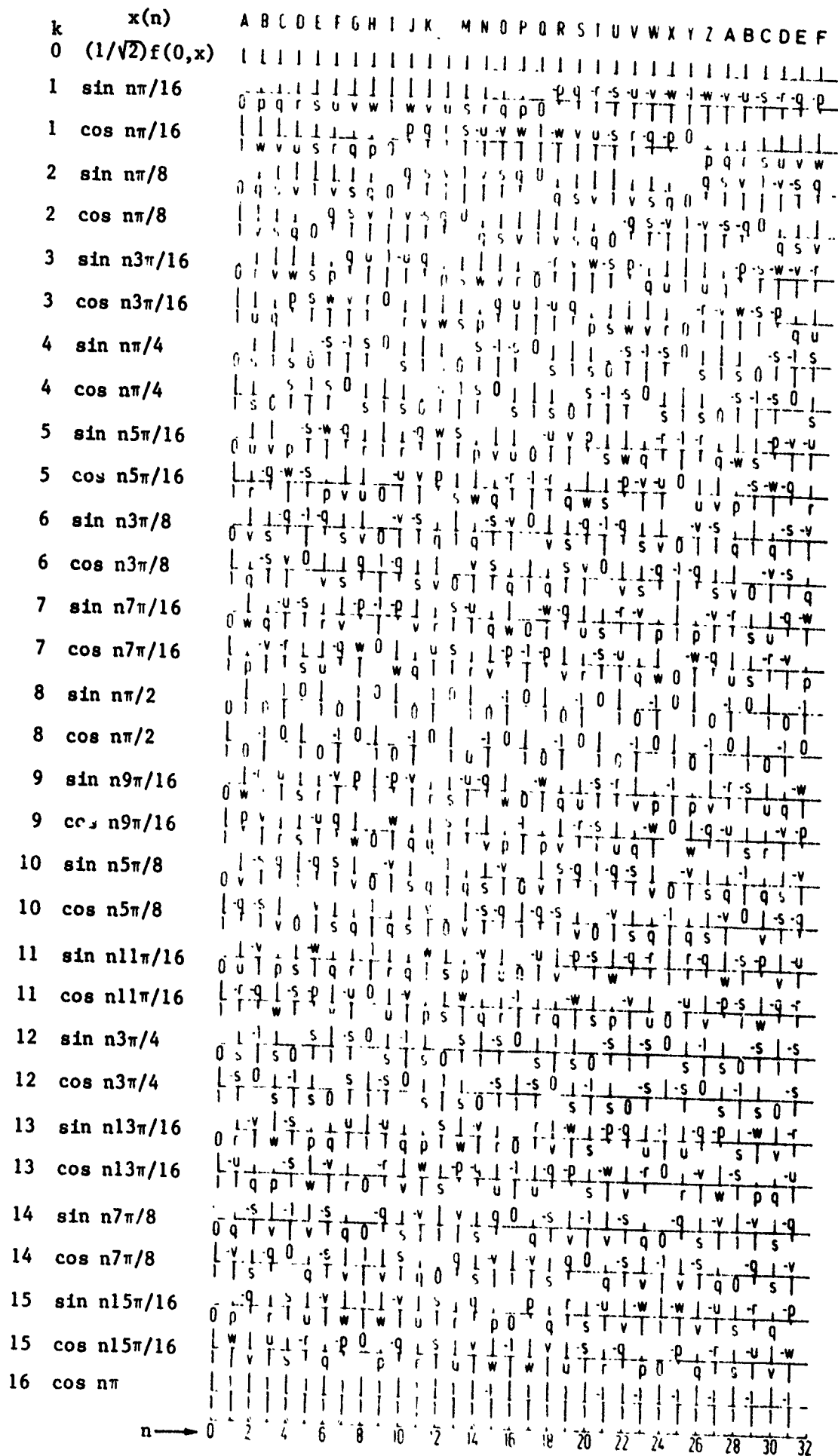
Figure A-2. The first 32 functions of the Fourier series represented by the samples derived from Figure A-1.

values of the sine and cosine terms in Equation (A-5) that multiply each x(n) for each beam k are shown in Figure A-2. This is shown in matrix form in Table A-1. Table A-2 takes advantage of some of the symmetry in Table A-1, by grouping four input channels multiplied by the same value of the trigonometry terms together. Table A-3 groups the terms in the upper portion of Table A-2 together to form four sums of four terms each. An analog circuit for implementing Table A-3 is shown in Figure A-3. The input signals at the left side of Figure A-3 correspond to the inputs at the top. of Table A-1. The outputs from the first stage of operational amplifiers corresponds to the sums at the top of Table A-2, while those of the second stage correspond to the sums at the top of Table A-3. The outputs of the last stage of operational amplifiers correspond to the final sums indicated by the lower portion of Table A-3.

N=64 Channels

For N=64, Equation (A-2) becomes

$$X(k) = \sum_{n=0}^{63} x(n) \left[\cos \frac{\pi}{32}kn - j \sin \frac{\pi}{32}kn \right] \tag{A-6}$$

$$k=0,1,2,\ldots,N-1$$

The values of the filter coefficients in Equation (A-6) are shown in Figure A-4. Table A-4 shows Equation (A-6) in a matrix format. Table A-5 shows the first level of simplification resulting in the first stage of operational amplifiers. Table A-6 shows the result of making four sums of four inputs each for the second stage of operational amplifiers providing a weighted sum of four of the outputs from the second stage of operational amplifiers is indicated by the lower portion of Table A-6.

An analog circuit implementing Table A-6 is shown in Figure A-5.

Table A-1. The values of the samples of the 32 functions of the Fourier series in Figure A-2. $p=\sin\pi/16$, $q=\sin\pi/8$, $r=\sin 3\pi/16$, $s=\sin\pi/4 = \sqrt{2}/2$, $u=\sin 5\pi/16$, $v=\sin 3\pi/8$, $w=\sin 7\pi/16$.

| n	x(n)	0	1	2	3	4	5	6	7	8	9	10	11	12	13	14	15	16	17	18	19	20	21	22	23	24	25	26	27	28	29	30	31
0	0	s	s	s	s	s	s	s	s	s	s	s	s	s	s	s	s	s	s	s	s	s	s	s	s	s	s	s	s	s	s	s	s
1	s1	0	p	q	r	s	u	v	w	1	w	v	u	s	r	q	p	0	-p	-q	-r	-s	-u	-v	-w	-1	-w	-v	-u	-s	-r	-q	-p
2	c1	1	w	v	u	s	r	q	p	0	-p	-q	-r	-s	-u	-v	-w	-1	-w	-v	-u	-s	-r	-q	-p	0	p	q	r	s	u	v	w
3	s2	0	q	s	v	1	v	s	q	0	-q	-s	-v	-1	-v	-s	-q	0	q	s	v	1	v	s	q	0	-q	-s	-v	-1	-v	-s	-q
4	c2	1	v	s	q	0	-q	-s	-v	-1	-v	-s	-q	0	q	s	v	1	v	s	q	0	-q	-s	-v	-1	-v	-s	-q	0	q	s	v
5	s3	0	r	v	w	s	p	-q	-u	-1	-u	-q	p	s	w	v	r	0	-r	-v	-w	-s	-p	q	u	1	u	q	-p	-s	-w	-v	-r
6	c3	1	u	q	-p	-s	-w	-v	-r	0	r	v	w	s	p	-q	-u	-1	-u	-q	p	s	w	v	r	0	-r	-v	-w	-s	-p	q	u
7	s4	0	s	1	s	0	-s	-1	-s	0	s	1	s	0	-s	-1	-s	0	s	1	s	0	-s	-1	-s	0	s	1	s	0	-s	-1	-s
8	c4	1	s	0	-s	-1	-s	0	s	1	s	0	-s	-1	-s	0	s	1	s	0	-s	-1	-s	0	s	1	s	0	-s	-1	-s	0	s
9	s5	0	u	v	p	-s	-w	-q	r	1	r	-q	-w	-s	p	v	u	0	-u	-v	-p	s	w	q	-r	-1	-r	q	w	s	-p	-v	-u
10	c5	1	r	-q	-w	-s	p	v	u	0	-u	-v	-p	s	w	q	-r	-1	-r	q	w	s	-p	-v	-u	0	u	v	p	-s	-w	-q	r
11	s6	0	v	s	-q	-1	-q	s	v	0	-v	-s	q	1	q	-s	-v	0	v	s	-q	-1	-q	s	v	0	-v	-s	q	1	q	-s	-v
12	c6	1	q	-s	-v	0	v	s	-q	-1	-q	s	v	0	-v	-s	q	1	q	-s	-v	0	v	s	-q	-1	-q	s	v	0	-v	-s	q
13	s7	0	w	q	-u	-s	r	v	-p	-1	-p	v	r	-s	-u	q	w	0	-w	-q	u	s	-r	-v	p	1	p	-v	-r	s	u	-q	-w
14	c7	1	p	-v	-r	s	u	-q	-w	0	w	q	-u	-s	r	v	-p	-1	-p	v	r	-s	-u	q	w	0	-w	-q	u	s	-r	-v	p
15	s8	0	1	0	-1	0	1	0	-1	0	1	0	-1	0	1	0	-1	0	1	0	-1	0	1	0	-1	0	1	0	-1	0	1	0	-1
16	c8	1	0	-1	0	1	0	-1	0	1	0	-1	0	1	0	-1	0	1	0	-1	0	1	0	-1	0	1	0	-1	0	1	0	-1	0
17	s9	0	w	-q	-u	s	r	-v	-p	1	-p	-v	r	s	-u	-q	w	0	-w	q	u	-s	-r	v	p	-1	p	v	-r	-s	u	q	-w
18	c9	1	-p	-v	r	s	-u	-q	w	0	-w	q	u	-s	-r	v	p	-1	p	v	-r	-s	u	q	-w	0	w	-q	-u	s	r	-v	-p
19	s10	0	v	-s	-q	1	-q	-s	v	0	-v	s	q	-1	q	s	-v	0	v	-s	-q	1	-q	-s	v	0	-v	s	q	-1	q	s	-v
20	c10	1	-q	-s	v	0	-v	s	q	-1	q	s	-v	0	v	-s	-q	1	-q	-s	v	0	-v	s	q	-1	q	s	-v	0	v	-s	-q
21	s11	0	u	-v	p	s	-w	q	r	-1	r	q	-w	s	p	-v	u	0	-u	v	-p	-s	w	-q	-r	1	-r	-q	w	-s	-p	v	-u
22	c11	1	-r	-q	w	-s	-p	v	-u	0	u	-v	p	s	-w	q	r	-1	r	q	-w	s	p	-v	u	0	-u	v	-p	-s	w	-q	-r
23	s12	0	s	-1	s	0	-s	1	-s	0	s	-1	s	0	-s	1	-s	0	s	-1	s	0	-s	1	-s	0	s	-1	s	0	-s	1	-s
24	c12	1	-s	0	s	-1	s	0	-s	1	-s	0	s	-1	s	0	-s	1	-s	0	s	-1	s	0	-s	1	-s	0	s	-1	s	0	-s
25	s13	0	r	-v	w	-s	p	q	-u	1	-u	q	p	-s	w	-v	r	0	-r	v	-w	s	-p	-q	u	-1	u	-q	-p	s	-w	v	-r
26	c13	1	-u	q	p	-s	w	-v	r	0	-r	v	-w	s	-p	-q	u	-1	u	-q	-p	s	-w	v	-r	0	r	-v	w	-s	p	q	-u
27	s14	0	q	-s	v	-1	v	-s	q	0	-q	s	-v	1	-v	s	-q	0	q	-s	v	-1	v	-s	q	0	-q	s	-v	1	-v	s	-q
28	c14	1	-v	s	-q	0	q	-s	v	-1	v	-s	q	0	-q	s	-v	1	-v	s	-q	0	q	-s	v	-1	v	-s	q	0	-q	s	-v
29	s15	0	p	-q	r	-s	u	-v	w	-1	w	-v	u	-s	r	-q	p	0	-p	q	-r	s	-u	v	-w	1	-w	v	-u	s	-r	q	-p
30	c15	1	-w	v	-u	s	-r	q	-p	0	p	-q	r	-s	u	-v	w	-1	w	-v	u	-s	r	-q	p	0	-p	q	-r	s	-u	v	-w
31	c16	1	-1	1	-1	1	-1	1	-1	1	-1	1	-1	1	-1	1	-1	1	-1	1	-1	1	-1	1	-1	1	-1	1	-1	1	-1	1	-1

Table A-2. Sums and differences of four samples A...F of the function F(k), and the values 0, +p, +q, +r, +s, +u, +v, +w, +1 of the samples of the first 32 functions of the Fourier series by which they are multiplied.

Table A-3. Sums and differences of 4^2 samples A...F of the function $X(n)$ multiplied with the values $+p$, $+q$, $+r$, $+s$, $+u$, $+v$, $+w$, $+1$ of the samples of the first 32 functions of the Fourier series, and the values 0, $+s$, $+1$ by which these weighted sums are multiplied.

Figure A-3. Circuit performing a Fourier transform of 32 input voltages at the terminals 0,1,...,31. A combination of fast Fourier transforms producing the sum of four or two voltages at a time is used.

$p = \sin \pi/16$
$q = \sin \pi/8$
$r = \sin 3\pi/16$
$s = \sin \pi/4 = \sqrt{}$
$u = \sin 5\pi/16$
$v = \sin 3\pi/8$
$w = \sin 7\pi/16$

R/p
R/q
R/r
R/s
R/u
R/v
R/w
R
R/2
R/4
R/8
special
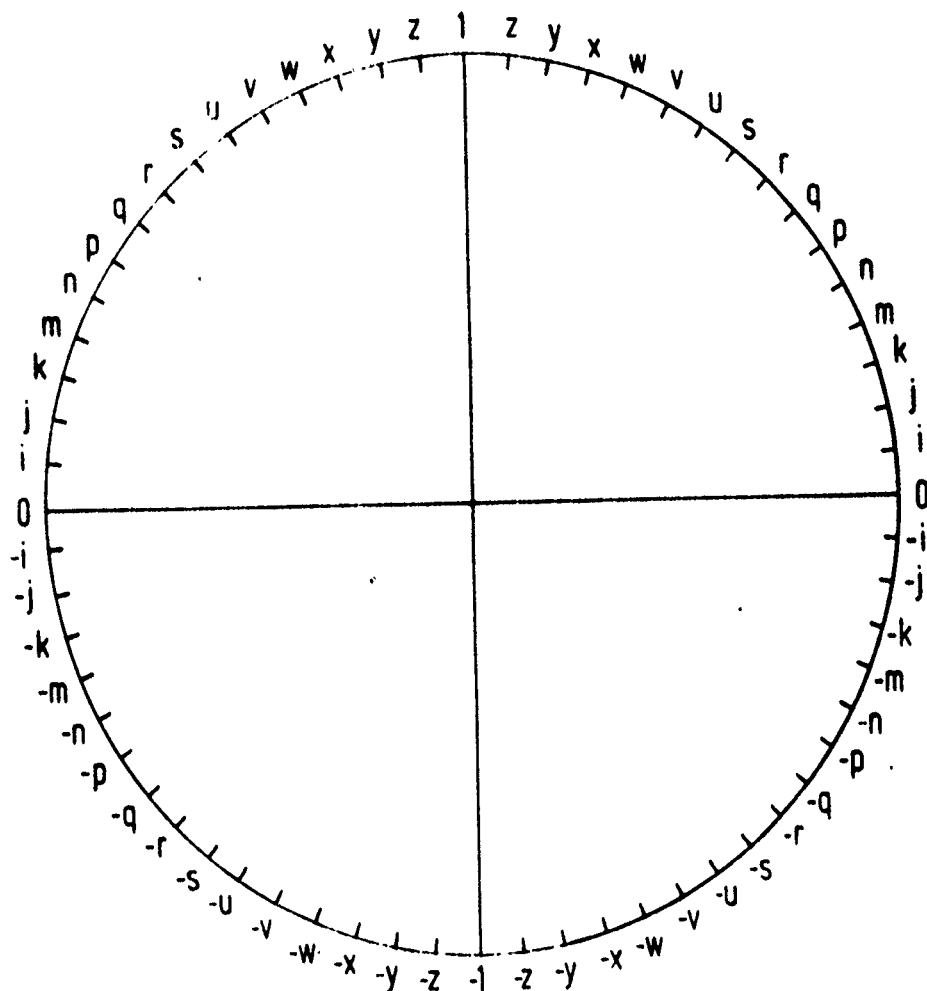
Figure A-4. Determination of the samples 0, ±i, ±j, ..., ±1 of the first 64 functions of the Fourier series. i=sinπ/32, j=sinπ/16, k=sin3π/32, m=sinπ/8, n=sin5π/32, p=sin3π/16, q=sin7π/32, r=sinπ/4= 2/2, s=sin4π/32, u=sin5π/16, v=sin11π/32, w=sin3π/8, x=sin13π/32, y=sin7π/16, z=sin15π/32.

Table A-4. The values of the samples of the first 64 functions of the Fourier series. The samples are continued to the right of column k=32 with equal signs for the symmetric functions (0, c1, c2, ..., c32) and with reversed signs for the skew-symmetric functions (s1, s2, ..., s31). See the caption of Figure A-4 for the values of the samples i, j, ..., z.

Table A-5b. 1 divisible by 2 but not by 4

Row	Equation				
95	$(P + \bar{L}) - (\bar{V} + J)$	15	47	31	63
94	$(O + \bar{U}) - (\bar{E} + K)$	14	46	30	62
93	$(N + \bar{T}) - (\bar{D} + J)$	13	45	29	61
92	$(M + \bar{S}) - (\bar{C} + I)$	12	44	28	60
91	$(L + \bar{R}) - (\bar{B} + H)$	11	43	27	59
90	$(K + \bar{Q}) - (\bar{A} + G)$	10	42	26	58
89	$(J + \bar{P}) - (\bar{Z} + F)$	9	41	25	57
88	$(I + \bar{O}) - (Y + E)$	8	40	24	56
87	$(H + \bar{N}) - (X + D)$	7	39	23	55
86	$(G + \bar{M}) - (W + C)$	6	38	22	54
85	$(F + \bar{L}) - (V + B)$	5	37	21	53
84	$(E + \bar{K}) - (U + A)$	4	36	20	52
83	$(D + \bar{J}) - (T + \bar{Z})$	3	35	19	51
82	$(C + \bar{I}) - (S + \bar{Y})$	2	34	18	50
81	$(B + \bar{H}) - (R + \bar{X})$	1	33	17	49
80	$(A + \bar{G}) - (Q + \bar{W})$	0	32	16	48

Column headers: s2, c2, s6, c6, s10, c10, s14, c14, s18, c18, s22, c22, s26, c26, s30, c30

Table A-5c. 1 odd, functions s1.

	Equation					s1	s3	s5	s7	s9	s11	s13	s15	s17	s19	s21	s23	s25	s27	s29	s31
111	$(P - \overline{V}) + (\overline{R} - \overline{X})$	15	47	17	49	z	-x	y	-s	q	-n	k	-i	-i	k	-n	q	-s	y	-x	z
110	$(O - \overline{U}) + (\overline{S} - \overline{Y})$	14	46	18	50	v	-u	p	-j	-j	p	-u	y	-y	u	-p	j	j	-p	u	-v
109	$(N - \overline{T}) + (\overline{T} - \overline{Z})$	13	45	19	51	x	-q	i	n	-v	z	-s	k	k	-s	z	-v	n	i	-q	x
108	$(M - \overline{S}) + (U - A)$	12	44	20	52	w	-m	-m	w	-w	m	m	-w	w	-m	-m	w	-w	m	m	-w
107	$(L - \overline{R}) + (V - B)$	11	43	21	53	v	-i	-s	x	-k	-q	z	-n	-n	z	-q	-k	x	-s	-i	v
106	$(K - \overline{Q}) + (W - C)$	10	42	22	54	u	j	-v	p	p	-v	j	u	-u	-j	v	-p	-p	v	-j	-u
105	$(J - \overline{P}) + (X - D)$	9	41	23	55	s	n	-x	-i	z	-k	-v	q	q	-v	-k	z	-i	-x	n	s
104	$(I - \overline{O}) + (Y - E)$	8	40	24	56	r	r	-r	-r	r	r	-r	-r	r	r	-r	-r	r	r	-r	-r
103	$(H - \overline{N}) + (Z - F)$	7	39	25	57	q	v	-k	-z	-i	x	n	-s	-s	n	x	-i	-z	-k	v	q
102	$(G - \overline{M}) + (A - G)$	6	38	26	58	p	y	j	-u	-u	j	y	p	-p	-y	-j	u	u	-j	-y	-p
101	$(F - \overline{L}) + (B - H)$	5	37	27	59	n	z	q	-k	-x	-s	i	v	v	i	-s	-x	-k	q	z	n
100	$(E - \overline{K}) + (C - I)$	4	36	28	60	m	w	w	m	-m	-w	-w	-m	m	w	w	m	-m	-w	-w	-m
99	$(D - \overline{J}) + (D - J)$	3	35	29	61	k	s	z	v	n	-i	-q	-x	-x	-q	-i	n	v	z	s	k
98	$(C - \overline{I}) + (E - K)$	2	34	30	62	j	p	u	y	y	u	p	j	-j	-p	-u	-y	-y	-u	-p	-j
97	$(B - \overline{H}) + (F - L)$	1	33	31	63	i	k	n	q	s	v	x	z	z	x	v	s	q	n	k	i
96	$Q - \overline{W}$	0	32	16	48	1	-1	1	-1	1	-1	1	-1	1	-1	1	-1	1	-1	1	-1

Table A-5c. 1 odd, functions s1.

Table A-5d. 1 odd, functions c1.

	c1	c3	c5	c7	c9	c11	c13	c15	c17	c19	c21	c23	c25	c27	c29	c31
112: A - G; 0 32 16 48	1	1	1	1	1	1	1	1	1	1	1	1	1	1	1	1
113: (B - H) - (E - L); 1 33 31 63	z	x	v	s	q	n	k	i	-i	-k	-n	-q	-s	-v	-x	-z
114: (C - I) - (E - K); 2 34 30 62	y	u	p	j	-j	-p	-u	-y	-y	-u	-p	-j	j	p	u	y
115: (D - J) - (D - J); 3 35 29 61	x	q	i	-n	-v	-z	-s	-k	k	s	z	v	n	-i	-q	-x
116: (E - K) - (C - I); 4 36 28 60	w	m	-m	-w	-w	-m	m	w	w	m	-m	-w	-w	-m	m	w
117: (F - L) - (B - H); 5 37 27 59	v	i	-s	-x	-k	q	z	n	-n	-z	-q	k	x	s	-i	-v
118: (G - M) - (A - G); 6 38 26 58	u	-j	-y	-p	p	y	j	-u	-u	-j	y	p	-p	-y	-j	u
119: (H - N) - (Z - F); 7 39 25 57	s	-n	-x	i	z	k	-v	-q	q	v	-k	-z	-i	x	n	-s
120: (I - O) - (Y - E); 8 40 24 56	r	-r	-r	r	r	-r	-r	r	r	-r	-r	r	r	-r	-r	r
121: (J - P) - (X - D); 9 41 23 55	q	-v	-k	z	-i	-x	n	s	-s	-n	x	i	-z	k	v	-q
122: (K - Q) - (W - C); 10 42 22 54	p	-y	j	u	-u	-j	y	-p	-p	y	-j	-u	u	j	-y	p
123: (L - R) - (V - B); 11 43 21 53	n	-z	q	k	-x	s	i	-v	v	-i	-s	x	-k	-q	z	-n
124: (M - S) - (U - A); 12 44 20 52	m	-w	w	-m	-m	w	-w	m	m	-w	w	-m	-m	w	-w	m
125: (N - T) - (T - Z); 13 45 19 51	k	-s	z	-v	n	i	-q	x	-x	q	-i	-n	v	-z	s	-k
126: (O - U) - (S - Y); 14 46 18 50	j	-p	u	-y	y	-u	p	-j	-j	p	-u	y	-y	u	-p	j
127: (P - V) - (R - X); 15 47 17 49	i	-k	n	-q	s	-v	x	-z	z	-x	v	-s	q	-n	k	-i

Table A-6a (Table A-6).

Column headers: 128, 129, 130, 131, 132, 133, 134, 135, 136, 137, 138, 139, 140, 141, 142, 143

Group formulas:

Column 128: (A+G+Q+W) + (E+K+U+A) + (I+Q+Y+E) + (M+S+C+I) (groups 64, 68, 72, 76)

Column 132: (B+H+R+X) + (F+L+V+B) + (J+P+Z+F) + (N+T+D+J) (groups 65, 69, 73, 77)

Column 136: (C+I+S+Y) + (G+M+W+C) + (K+Q+A+G) + (O+U+E+K) (groups 66, 70, 74, 78)

Column 140: (D+J+T+Z) + (H+N+X+D) + (L+R+B+H) + (P+V+F+L) (groups 67, 71, 75, 79)

		128	129	130	131	132	133	134	135	136	137	138	139	140	141	142	143
192	0	r				r				r				r			
193	s 4			1				m				r				w	
194	c 4				1			w				r					m
195	s 8					r					1				r		
196	c 8		1			r									-r		
197	s12			-1				w				r				-m	
198	c12				1			m					-r				-w
199	s16					1								-1			
200	c16	1								-1							
201	s20			1				w				-r				-m	
202	c20				1			-m					-r				w
203	s24		1			r					-1					r	
204	c24					-r										r	
205	s28			-1				m				-r				w	
206	c28				1			-w					r				-m
207	c32	1				-1				1				-1			

Table A-6. Sums and differences of 4^2 samples A...L of the function X(n) multiplied with the values ±i, ±j, ..., ±1 of the samples of the first 64 functions of the Fourier series, and the values ±m, ±r, ±w, ±1 by which the weighted sums are multiplied. The table is arranged in four parts that correspond to the four parts of Table A-5.

Table A-6a

Table A-6b is a large sparse matrix. The header row numbers (left to right) are:

144, 145, 152, 153, 146, 147, 154, 155, 148, 149, 150, 151, 156, 157, 158, 159, 148a, 149a, 150a, 151a, 156a, 157a, 158a, 159a

- $R4$ / $R8$ / 92 — $r(A+G-Q-W) + r(B+K-U-A) + (I+O-V-E) + r(M+S-C-J)$
- 86 / 90 / 91 — $m(C+I-S-Y) + w(G+M-W-C) + w(K+Q-A-G) + m(O+U-E-K)$
- $R1$ / $R5$ / $R7$ — $J(A+H-R-X) + p(D+J-T-Z) + u(F+L-V-B) + y(H+N-V-D)$
- $R9$ / 93 / 95 — $y(J+P-Z-F) + w(L+R-B-H) + p(N+T-D-J) + J(P+V-F-L)$

Row	Label	144	145	152	153	146	147	154	155	148	149	150	151	156	157	158	159	148a	149a	150a	151a	156a	157a	158a	159a
208	s 2	1				1				1								1							
209	s 6		1			1					1								1						
210	s10		-1			1														1					
211	s14	-1				1															1				
212	s18	1				-1						1									1				
213	s22		1			-1						1								1					
214	s26		-1			-1				1								1							
215	s30	-1				-1				1								1							
216	c 2		1			1					1												1		
217	c 6			1			1						1										1		
218	c10			1			-1							1						1					
219	c14				1		-1								1									1	
220	c18				1		-1									-1				-1					-2
221	c22			1			-1									-1									-1
222	c26			1						1		-1												-1	
223	c30				1		1										-1							-1	

Table A-6b

Table A-6c

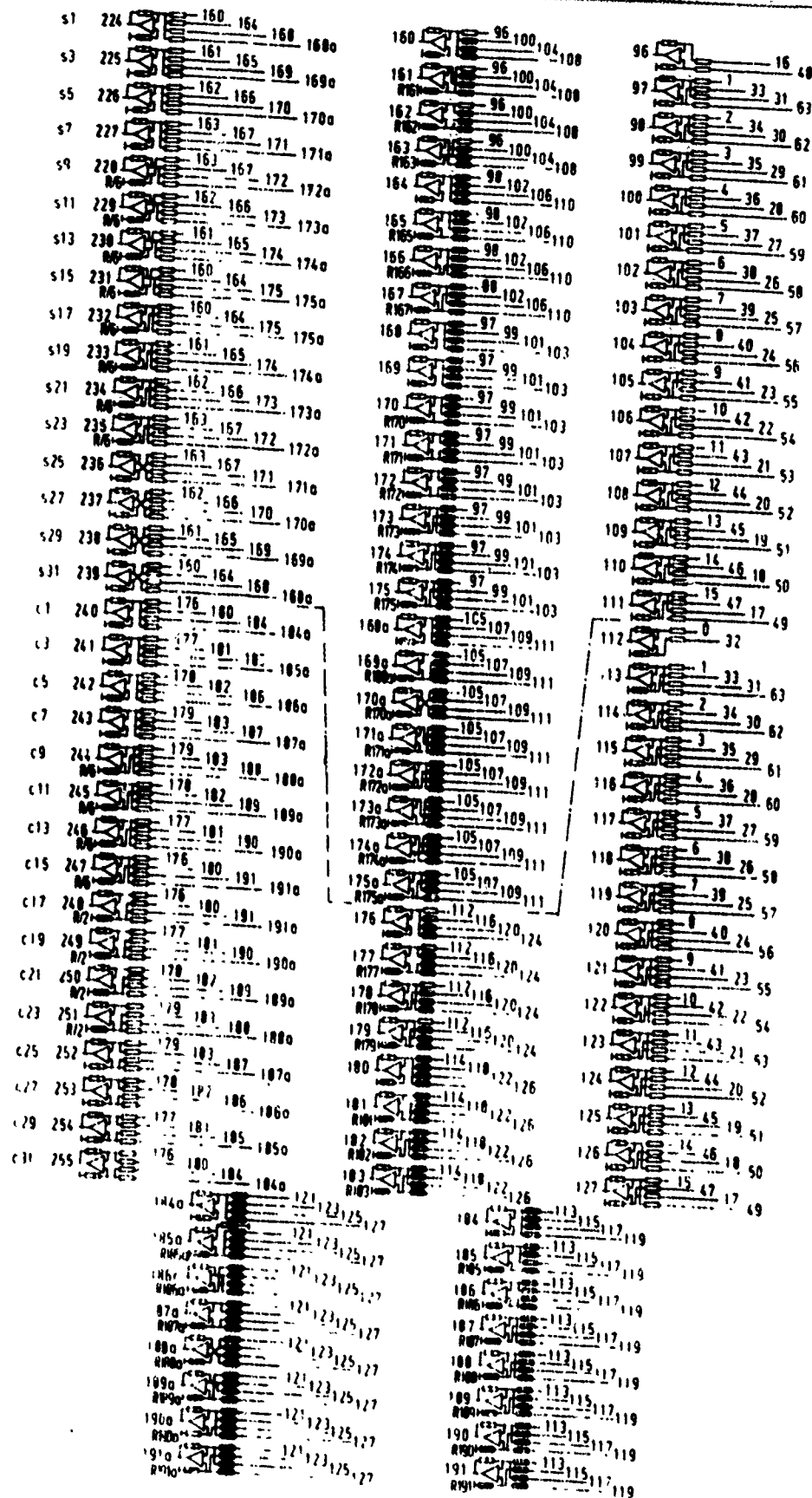|		160	161	162	163	164	165	166	167	168	169	170	171	172	173	174	175	168a	169a	170a	171a	172a	173a	174a	175a
224	s1	1			1					1															
225	s3		1			1												1							
226	s5			1			1			1									1						
227	s7				1			1			1									1					
228	s9				-1			1													1				
229	s11			-1			1					1										1			
230	s13		-1			1							1										1		
231	s15	-1				1								1										1	
232	s17	1			-1									1											1
233	s19		1		-1										1										1
234	s21			1		-1							1											1	
235	s23			1			-1							1									1		
236	s25			-1			-1						1								1				
237	s27		-1			-1						1									1				
238	s29		-1			-1					1								1						
239	s31	-1				-1				1							1								

Table A-6d

Figure A-5. Circuit performing a Fourier transform of 64 input voltages at the input terminals 0...63. The transformed voltages are obtained at the terminals 192...255.
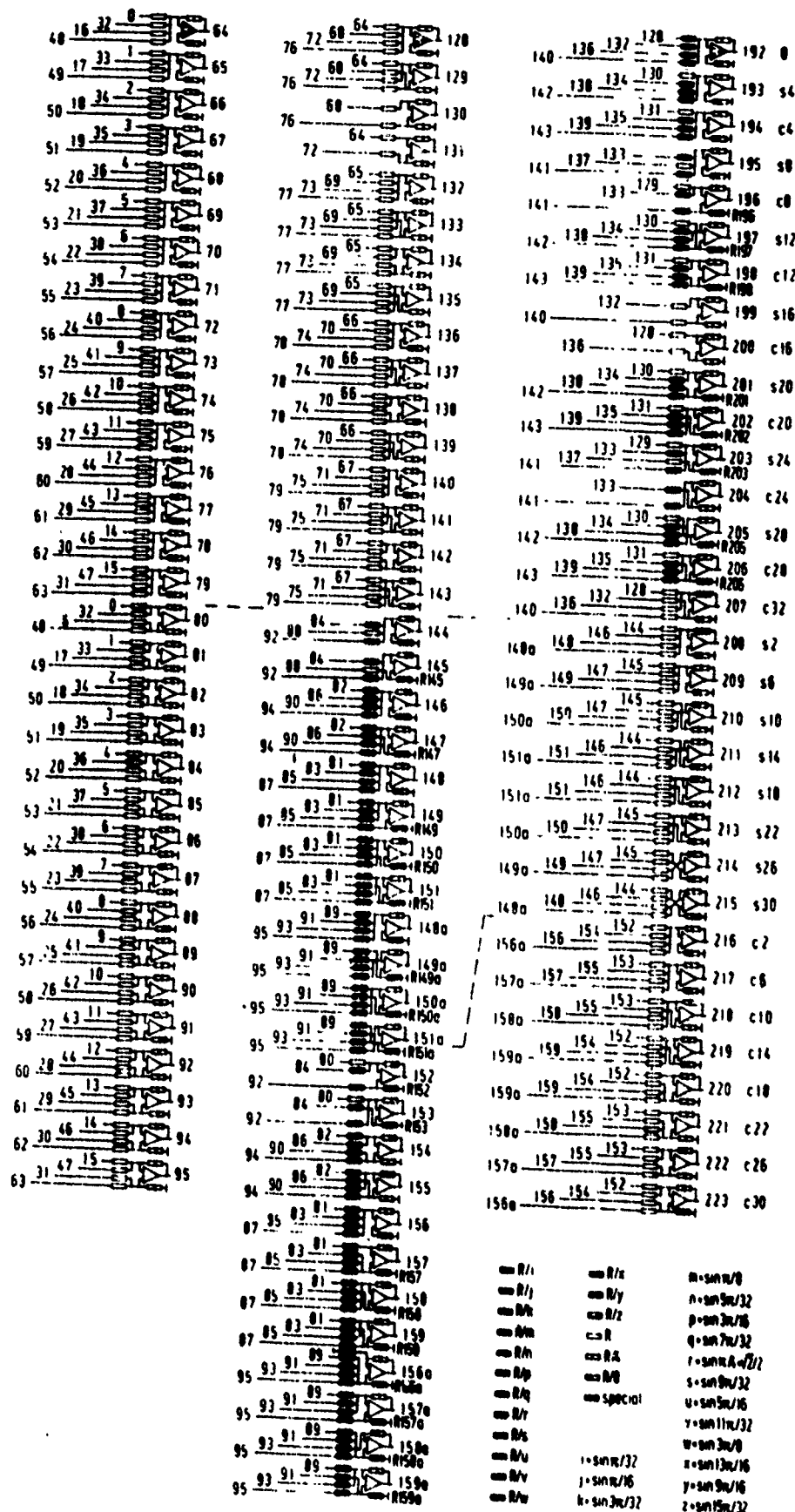
Figure A-5 (Continued)

APPENDIX B

BEAM AMBIGUITY RESOLUTION

This appendix derives the beam pattern output of a line array of N equally spaced hydrophones. The input channels are assumed to be processed with a discrete Fourier transform filter, and the left-right beam ambiguity is resolved by phase shifting the transformed imaginary term by 90° and adding it to the corresponding real-term as discussed in Section 2.3.

The discrete Fourier transform of the N input channels as implemented by the analog FFT circuit is given by

$$X(k,t) = \sum_{n=0}^{N-1} x(n,t) \, \varepsilon^{-j\frac{2\pi}{N}kn} \qquad\qquad k=0,1,2,\ldots,N-1 \quad \text{(B-1)}$$

$$= \sum_{n=0}^{N-1} x(n,t) \cos \frac{2\pi}{N}kn \; -j\sum_{n=0}^{N-1} x(n,t) \sin \frac{2\pi}{N}kn \qquad \text{(B-2)}$$

where n is the input channel index and k is the output beam index.

If the input data is real, then beam k will be the complex conjugate of beam (N-k-1). That is

$$X(P,t) = X(Q,t) \qquad\qquad\qquad\qquad\qquad\qquad \text{(B-3)}$$

where

$$X(P,t) = \sum_{n=0}^{N-1} x(n,t) \cos \frac{2\pi}{N}Pn \; +j\sum_{n=0}^{N-1} x(n,t) \sin \frac{2\pi}{N}Pn \qquad \text{(B-4)}$$

$$X(Q,t) = \sum_{n=0}^{N-1} x(n,t) \cos \frac{2\pi}{N} Pn \quad -j \sum_{n=0}^{N-1} x(n,t) \sin \frac{2\pi}{N} Pn \qquad (B-5)$$

where P=k and Q = N-k-1.

The beam ambiguity resolver circuit of Figure 2-5 integrates the imaginary term in Equation (B-4) or (B-5) and adds it to the real-term to obtain the following output beams:

$$X(P,t) = \sum_{n=0}^{N-1} x(n,t) \cos \frac{2\pi}{N} Pn \quad + \int \sum_{n=0}^{N-1} x(n,t) \sin \frac{2\pi}{N} Pn \, dt$$

$$(B-6)$$

$$X(Q,t) = \sum_{n=0}^{N-1} x(n,t) \cos \frac{2\pi}{N} Pn \quad - \int \sum_{n=0}^{N-1} x(n,t) \sin \frac{2\pi}{N} Pn \, dt$$

$$(B-7)$$

Assuming that the input signal is some general narrowband signal as

$$x(n,t) \doteq \cos \left[wt + \phi(n) \right] \qquad (B-8)$$

and that the integration of this signal is amplitude scaled such that

$$\int x(n,t) = \sin \left[wt + \phi(n) \right] \qquad (B-9)$$

then by substitution and by bringing the integral signs inside the summations, Equations (B-6) and (B-7) become

$$X(P,t) = \sum_{n=0}^{N-1} \cos\left[wt + \phi(n)\right] \cos \frac{2\pi}{N}Pn$$

$$+ \sum_{n=0}^{N-1} \sin\left[wt + \phi(n)\right] \sin \frac{2\pi}{N}Pn \qquad \text{(B-10)}$$

$$X(Q,t) = \sum_{n=0}^{N-1} \cos\left[wt + \phi(n)\right] \cos \frac{2\pi}{N}Pn$$

$$- \sum_{n=0}^{N-1} \sin\left[wt + \phi(n)\right] \sin \frac{2\pi}{N}Pn \qquad \text{(B-11)}$$

By using standard trigonometry identities, Equation (B-10) becomes

$$X(P,t) = \sum_{n=0}^{N-1} \cos\left[wt + \phi(n) - \frac{2\pi}{N}Pn\right] \qquad \text{(B-12)}$$

For uniformly spaced hydrophones and plane waves (i.e. $\phi(n) = n\phi$) this becomes

$$X(P,t) = \cos\left[wt + \frac{N-1}{2}\left(\phi - \frac{2\pi}{N}P\right)\right] \frac{\sin\left[\frac{N}{2}\left(\phi - \frac{2\pi}{N}P\right)\right]}{\sin\left[\frac{1}{2}\left(\phi - \frac{2\pi}{N}P\right)\right]} \qquad \text{(B-13)}$$

The beam pattern function for this beam becomes

$$\left[\frac{X(P,t)}{N}\right]^2 = \left[\frac{\sin\left[N\left(\phi - \frac{2\pi}{N}P\right)/2\right]}{N\sin\left[\left(\phi - \frac{2\pi}{N}P\right)/2\right]}\right]^2 \left[\cos\left[wt + \frac{N-1}{2}\left(\phi - \frac{2\pi}{N}P\right)\right]\right]^2$$

$$\text{(B-14)}$$

which Urick shows is the beam pattern function expected for a line array of uniformly spaced hydrophones. The main beam pointing direction for Equation (B-14) are those angles, ϕ, for which $\phi = \frac{2\pi}{N}P$.

Following the same approach, Equation (B-11) can be shown to equal

$$X(Q,t) = \sum_{n=0}^{N-1} \cos\left[wt + \left(\phi + \frac{2\pi}{N}P\right)n\right] \tag{B-15}$$

The beam pattern function for Equation (B-15) is

$$\left[\frac{X(Q,t)}{N}\right]^2 = \left[\frac{\sin\left[N\left(\phi + \frac{2\pi}{N}P\right)/2\right]}{N\sin\left[\left(\phi + \frac{2\pi}{N}P\right)/2\right]}\right]^2 \left[\cos\left[wt + \frac{N-1}{2}\left(\phi + \frac{2\pi}{N}P\right)\right]\right]^2 \tag{B-16}$$

Equation (B-16) has main beam pointing directions, ϕ, equal to $\phi = -\frac{2\pi}{N}P$.

Therefore, the ambiguity resolution circuit of Figure 2-5 will resolve the ambiguity of beams on opposite sides of broadside, forming N unique beams for a beamformer with N input channels of real data.